EMILIN1 deficiency causes arterial tortuosity with osteopenia and connects impaired elastogenesis with defective collagen fibrillogenesis

Graphical abstract

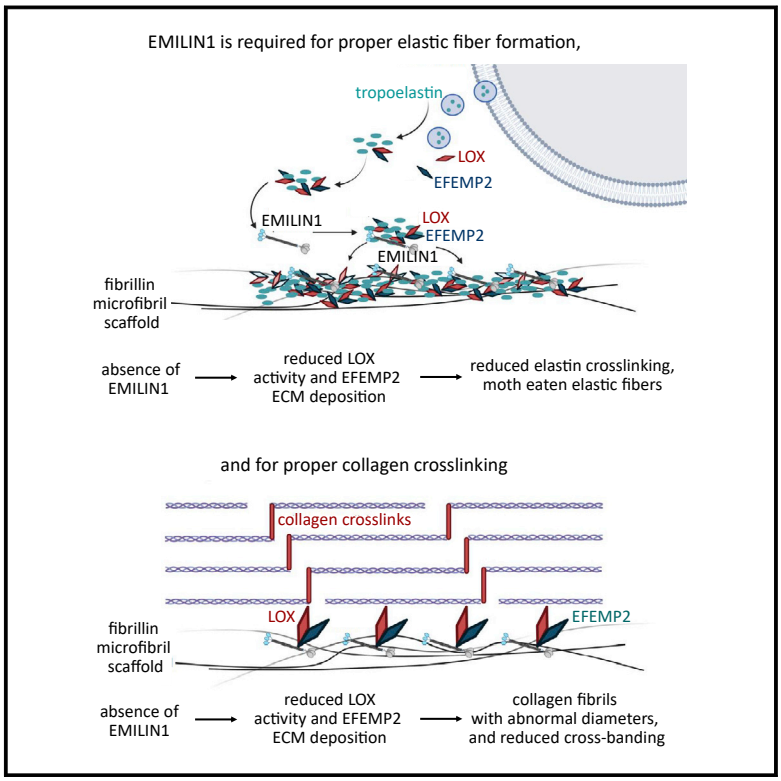

Authors

Christin S. Adamo, Aude Beyens, Alvise Schiavinato, ..., Lynn Y. Sakai, Gerhard Sengle, Bert Callewaert

Correspondence

gsengle@uni-koeln.de (G.S.), bert.callewaert@ugent.be (B.C.)

Adamo et al. describe a cutis laxa syndrome caused by bi-allelic loss-of-function variants in *EMILIN1* characterized by arterial tortuosity, aneurysm formation, and osteopenia. They provide a model in which EMILIN1 connects elastic fiber network with collagen fibril formation, relevant for both bone and vascular tissue homeostasis.

Adamo et al., 2022, The American Journal of Human Genetics *109*, 2230–2252
December 1, 2022
https://doi.org/10.1016/j.ajhg.2022.10.010

CellPress

ARTICLE

EMILIN1 deficiency causes arterial tortuosity with osteopenia and connects impaired elastogenesis with defective collagen fibrillogenesis

Christin S. Adamo,[1,2,36] Aude Beyens,[3,4,5,36] Alvise Schiavinato,[1,6] Douglas R. Keene,[7] Sara F. Tufa,[7] Matthias Mörgelin,[8,9] Jürgen Brinckmann,[10] Takako Sasaki,[11] Anja Niehoff,[12,13] Maren Dreiner,[13] Lore Pottie,[3,4] Laura Muiño-Mosquera,[3,14] Elif Yilmaz Gulec,[15,16] Alper Gezdirici,[17] Paola Braghetta,[18] Paolo Bonaldo,[18] Raimund Wagener,[1] Mats Paulsson,[1,12,19] Helen Bornaun,[20] Riet De Rycke,[21,22] Michiel De Bruyne,[21,22] Femke Baeke,[21,22] Walter P. Devine,[23] Balram Gangaram,[24] Allison Tam,[24] Meena Balasubramanian,[25,26,27] Sian Ellard,[28] Sandra Moore,[28] Sofie Symoens,[3,4] Joseph Shen,[29] Stacey Cole,[29] Ulrike Schwarze,[30] Kathryn W. Holmes,[31] Susan J. Hayflick,[32] Wojciech Wiszniewski,[32] Sheela Nampoothiri,[33] Elaine C. Davis,[34] Lynn Y. Sakai,[32] Gerhard Sengle,[1,2,12,19,35,37,*] and Bert Callewaert[3,4,35,37,*]

Summary

EMILIN1 (elastin-microfibril-interface-located-protein-1) is a structural component of the elastic fiber network and localizes to the interface between the fibrillin microfibril scaffold and the elastin core. How EMILIN1 contributes to connective tissue integrity is not fully understood. Here, we report bi-allelic *EMILIN1* loss-of-function variants causative for an entity combining cutis laxa, arterial tortuosity, aneurysm formation, and bone fragility, resembling autosomal-recessive cutis laxa type 1B, due to *EFEMP2* (*FBLN4*) deficiency. In both humans and mice, absence of EMILIN1 impairs EFEMP2 extracellular matrix deposition and LOX activity resulting in impaired elastogenesis, reduced collagen crosslinking, and aberrant growth factor signaling. Collagen fiber ultrastructure and histopathology in EMILIN1- or EFEMP2-deficient skin and aorta corroborate these findings and murine *Emilin1*$^{-/-}$ femora show abnormal trabecular bone formation and strength. Altogether, EMILIN1 connects elastic fiber network with collagen fibril formation, relevant for both bone and vascular tissue homeostasis.

Introduction

Elastogenesis is a complex multi-step process in which tropoelastin is incorporated into fibrillin microfibril (FMF) bundles and crosslinked by lysyl oxidase (LOX) to generate elastic fibers.[1] In elastic fibers, EMILIN1 (elastin-microfibril-interface-located-protein-1) localizes at the interface between the FMF scaffold and the elastin core.[2,3] EMILIN1 is a 115 kDa glycoprotein and belongs to the EMILIN/Multimerin family which is characterized by a

[1]Department of Pediatrics and Adolescent Medicine, Faculty of Medicine and University Hospital Cologne, University of Cologne, 50931 Cologne, Germany; [2]Center for Biochemistry, Faculty of Medicine and University Hospital Cologne, University of Cologne, 50931 Cologne, Germany; [3]Center for Medical Genetics, Ghent University Hospital, 9000 Ghent, Belgium; [4]Department of Biomolecular Medicine, Ghent University, 9000 Ghent, Belgium; [5]Department of Dermatology, Ghent University Hospital, 9000 Ghent, Belgium; [6]Istituto Di Patalogia Clinica, Azienda Sanitaria Universitaria Integrata di Udine (ASUID), 33100 Udine, Italy; [7]Research Division, Shriners Hospital for Children, Portland, OR 97239, USA; [8]Division of Infection Medicine, Department of Clinical Sciences, Lund University, 22242 Lund, Sweden; [9]Colzyx AB, 22363 Lund, Sweden; [10]Department of Dermatology and Institute of Virology and Cell Biology, University of Lübeck, 23562 Lübeck, Germany; [11]Department of Biochemistry II, Faculty of Medicine, Oita University, Oita 870-1192, Japan; [12]Cologne Center for Musculoskeletal Biomechanics (CCMB), Medical Faculty and University Hospital Cologne, University of Cologne, 50931 Cologne, Germany; [13]Institute of Biomechanics and Orthopaedics, German Sport University Cologne, 50933 Cologne, Germany; [14]Department of Pediatric Cardiology, Ghent University Hospital, 9000 Ghent, Belgium; [15]Department of Medical Genetics, Istanbul Medeniyet University Medical School, 34720 Istanbul, Turkey; [16]Department of Medical Genetics, Istanbul Goztepe Prof. Dr. Suleyman Yalcin City Hospital, 34722 Istanbul, Turkey; [17]Department of Medical Genetics, Basaksehir Cam and Sakura City Hospital, 34480 Istanbul, Turkey; [18]Department of Molecular Medicine, University of Padova, 35131 Padova, Italy; [19]Center for Molecular Medicine Cologne (CMMC), University of Cologne, 50931 Cologne, Germany; [20]Department of Pediatric Cardiology, Kanuni Sultan Suleyman Research and Training Hospital, 34303 Istanbul, Turkey; [21]Department of Biomedical Molecular Biology Ghent University, 9000 Ghent, Belgium; [22]VIB Center for Inflammation Research and BioImaging Core, VIB, 9052 Ghent, Belgium; [23]Department of Pathology, University of California San Francisco, San Francisco, CA 94115, USA; [24]Division of Genetics, Department of Pediatrics, University of California San Francisco, San Francisco, CA 94158, USA; [25]Highly Specialised Osteogenesis Imperfecta Service, Sheffield Children's Hospital NHS Foundation Trust, Sheffield S10 2TH, UK; [26]Department of Oncology and Metabolism, The University of Sheffield, Sheffield S10 2TN, UK; [27]Sheffield Clinical Genetics Service, Sheffield Children's NHS Foundation Trust, Sheffield S10 2TH, UK; [28]Exeter Genomics Laboratory, Royal Devon and Exeter NHS Foundation Trust, Exeter EX2 5DW, UK; [29]Division of Genomic Medicine, Department of Pediatrics, MIND Institute, University of California Sacramento, Sacramento, CA 95817, USA; [30]Departments of Pathology and Medicine (Medical Genetics), University of Washington, Seattle, WA, USA; [31]Department of Pediatrics, Oregon Health & Science University, Portland, OR 97239, USA; [32]Department of Molecular and Medical Genetics, Oregon Health & Science University, Portland, OR 97239, USA; [33]Department of Pediatric Genetics, Amrita Institute of Medical Sciences and Research Center, Cochin, Kerala 682041, India; [34]Department of Anatomy and Cell Biology, McGill University, Montreal, QC H3A 0C7, Canada
[35]Senior authors
[36]These authors contributed equally
[37]These authors contributed equally
*Correspondence: gsengle@uni-koeln.de (G.S.), bert.callewaert@ugent.be (B.C.)
https://doi.org/10.1016/j.ajhg.2022.10.010.

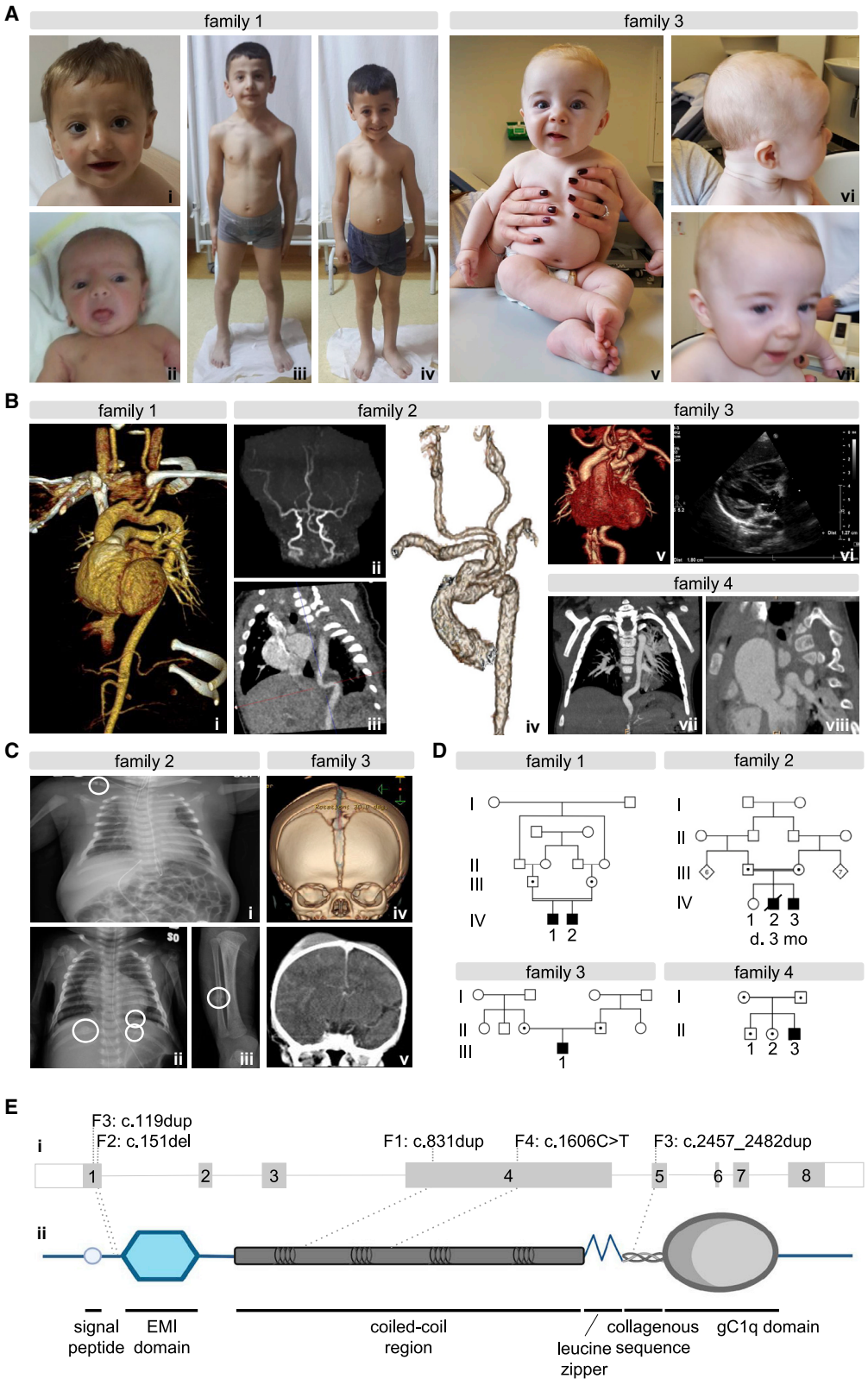

Figure 1. Clinical and molecular characteristics of affected individuals with *EMILIN1* variants

(A) Clinical pictures of F1:IV-1 (i, age 3 years; iii, age 7 years), F1:IV-2 (ii, age 3 months; iv, age 5 years), and F3:III-1 (v, vi, vii, age 3 months). Craniofacial features are mild and include downslanted palpebral fissures, epicanthal folds, a convex and/or broad nasal ridge and tip, long and flat philtrum, thin upper lip, and micrognathia.

(B) Vascular imaging studies. i. 3D vascular imaging in F1:IV-1 showing arterial tortuosity and aortic root dilatation (frontal view). ii–iv. MR angiography and 3D vascular imaging indicating severe tortuosity of the aorta, intracranial, pulmonary, and carotid arteries in F2:IV-2 (axial, left sagittal, and frontal view). v–vi. Aortic aneurysm and tortuosity illustrated with CT rendering images (frontal view)

(legend continued on next page)

defined domain structure: an N-terminal EMI domain, a cysteine-rich sequence of about 80 amino acids, a central part of about 700 amino acids with high probability of coiled-coil structures, and a C-terminal region homologous to the gC1q domain.[4]

The precise role of EMILIN1 in elastogenesis remains obscure. EMILIN1 interacts directly with EFEMP2 (also known as fibulin-4) and is required for proper extracellular matrix (ECM) deposition of EFEMP2.[5] In vascular smooth muscle cell cultures, anti-EMILIN1 antibodies inhibit elastin deposition,[2] while pull-down experiments suggest a direct interaction with ELN and FBLN5, a FMF-associated protein that assists in tropoelastin deposition onto FMF.[6,7] Genetic ablation of *Emilin1* in mice causes elastic fiber defects in aorta and skin resulting in vascular abnormalities such as increased blood pressure, increased peripheral vascular resistance, and reduced vessel size.[6,8]

Impaired elastogenesis has severe consequences in elastin-rich tissues, including the skin and cardiovascular and pulmonary system. For instance, heterozygous C-terminal frameshift variants in *ELN* (MIM: 130160) produce aberrant tropoelastin and cause autosomal-dominant cutis laxa (ADCL [MIM: 123700]),[9–12] showing skin redundancy and a risk for emphysema and aortic root dilatation.[9,10,12] Also, deficiency of FMF-associated EFEMP2, caused by pathogenic variants in *EFEMP2* (*FBLN4*, MIM: 604633), results in autosomal-recessive cutis laxa type 1B (ARCL1B [MIM: 614437]) characterized by both elongated and tortuous arteries that are prone to aneurysm formation and dissection and also variable osteoporosis.[13,14] Ablation of EFEMP2 in mice inhibits elastogenesis in all elastic tissues leading to perinatal death.[15] EFEMP2 interacts with the LOX propeptide and targets LOX to FMF, where its activation occurs after propeptide removal.[16] Mature LOX establishes collagen crosslinks, which is essential for tissue integrity and tensile strength.[17] Recently, a heterozygous *EMILIN1* (Genbank NM_007046.4; ENST00000380320.9; MIM: 130660) variant affecting the signal peptidase cleavage site (c.64G>A [p.Ala22Thr]) has been reported in a family exhibiting ascending and descending aortic aneurysms, increased skin elasticity, arthropathy, and bilateral lower limb peripheral neuropathy.[18] Another study reported a c.748C>T (p.Arg250Cys) variant located in the coiled-coil region of EMILIN1 in a family with distal motor neuropathy and presence of a disorganized ECM network upon nerve biopsy.[19] Both variants associated with a disorganized ECM network in skin biopsies. Although these findings point to EMILIN1 involvement in connective tissue homeostasis, the precise role in human disease remains enigmatic.

Here, we report homozygous *EMILIN1* loss-of-function variants that impair both elastin and collagen fiber formation and cause a syndrome characterized by arterial tortuosity, aortic aneurysm formation, and bone fragility, reminiscent of ARCL1B. Biochemical analysis of fibroblast cultures and biopsies from affected individuals and corresponding *Emilin1*$^{-/-}$ mice indicate that EMILIN1 affects collagen fiber formation and crosslinking by controlling EFEMP2 ECM deposition and LOX function. Our findings significantly shed light on how the elastic fiber network impacts collagen fiber formation and homeostasis in the context of human disease.

Subjects and methods

Clinical assessment

Informed consents were obtained from all individuals or from their parents for minors, including permission to publish the clinical pictures in Figure 1. Case reports and all evaluated clinical features are summarized in the supplemental notes and Table S1. Individuals were evaluated at one of the referral centers and skin biopsies were obtained from affected individuals or carriers for fibroblast culture (F1:IV-1, F1:IV-2, F3:III-1, F4:II-3) and transmission electron microscopy (TEM) (F1:IV-1, F3:III-1, F4:I-1, F4:II-2, F4:II-3). Aortic tissue for histology and immunohistochemistry from individual F2:IV-2 was derived during surgery. Additionally, we obtained skin or aortic biopsies for the same purposes from individuals with bi-allelic pathogenic *EFEMP2* variants and age- and sex-matched control subjects. This study was conducted in accordance with the declaration of Helsinki and approved by the Ghent University Hospital (registration numbers B670201319336 and B6702020000194) and Oregon Health & Science University internal review board.

Exome sequencing

Exome sequencing (ES) was performed on genomic DNA (gDNA) extracted from blood leukocytes (F1:IV-1, F1:IV-2, F2:IV-2, F2:IV-3, F4:II-3) or skin fibroblasts (F3:III-1) of each individual. gDNA was enriched using the SureselectXT Human All Exon v6 kit (Agilent Technologies,), followed by sequencing on a HiSeq 3000 platform (Illumina). *EMILIN1* (Genbank: NM_007046.4) nucleotides were numbered according to the Human Genome

and echocardiography in F3:III-1. vii–viii: Giant and progressive aortic aneurysm in F4:II-3 upon CT imaging (frontal and left sagittal views).
(C) Conventional radiography and CT imaging showing fractures in most affected individuals (frontal views). i–iii: F2:IV-3 presenting with a fracture of the right clavicle and his older sibling F2:IV-2 presenting with bilateral fractures of the lower ribs and fibula. iv–v: F3:III-1 presenting with bilateral skull fractures.
(D) Pedigree analysis of affected individuals in four unrelated families carrying *EMILIN1* variants confirms segregation of the variants with the phenotype.
(E) Schematic representation of the identified variants in *EMILIN1* and corresponding protein in four unrelated families. i: Genomic position of each variant indicated within the exon structure of *EMILIN1*. ii. Schematic representation of the domains of EMILIN1, consisting of an N-terminal cysteine-rich EMI domain, followed by a coiled-coil structure, a leucine zipper motif, a short collagenous region, and a C-terminal gC1q domain. Alterations in protein domain structure are indicated correspondingly.

Variation Society guidelines with nucleotide A of the ATG start codon = c.1. The following algorithms were used to predict the consequences of variants identified by ES: Polyphen-2, PhD-SNP, SIFT, SNAP, MAPP, and REVEL. Allele frequencies were evaluated using the gnomAD population database. Variant confirmation and segregation analyses were performed with Sanger sequencing.

Animals

This study was carried out in strict accordance with the German federal law on animal welfare, and the protocols were approved by the "Landesamt für Natur, Umwelt und Verbraucherschutz Nordrhein-Westfalen" for breeding (permit No §4.19.013). The generation and genotyping of *Emilin1*$^{-/-}$ mice was previously described.[6] *Emilin1*$^{-/-}$ mice and wild-type littermates were maintained on a C57BL/6NCrl genetic background and sacrificed at indicated ages.

Antibodies

The following primary antibodies and dilutions were used for western blot (WB), immunohistochemistry (IHC), or immunofluorescence (IF) analysis: anti-Phospho-Smad2 (#ab3849, Merck Millipore, IHC: 1:200), anti-CTGF (#ab6992, Abcam, IHC: 1:200 dilution), anti-FN1 (#ab23750, Abcam, WB, IF: 1:1000), anti-collagen I (#ab34710, Abcam, WB: 1:500, IF: 1:50), and anti-LOX (#ab31238 and #ab174316, Abcam, WB: 1:500, IF: 1:200). Polyclonal rabbit anti-FBN1 antiserum (WB: 1:2,000, IF: 1:1,000) was raised against the recombinantly produced N-terminal half of human FBN1 (F90).[20] Polyclonal rabbit anti-EMILIN1 antiserum was raised against a recombinant fragment (Gly173–Gly815),[3] a rabbit monoclonal antibody detecting N-terminal residues of EMILIN1 was obtained from Abcam (#ab185953, WB: 1:500). Polyclonal rabbit antibodies recognizing mouse and human EFEMP2 (WB, IF: 1:1,000), as well as a monoclonal antibody recognizing human EFEMP2 used for immunogold labeling were generated as previously described.[21,22] Polyclonal rabbit anti-LTBP1 antiserum (IF: 1:1,000) was raised against the last 214 C-terminal residues of human LTBP1 (Arg1181–Glu1394) L1K.[23] Polyclonal rabbit anti-FBN2 antibody was raised against the C-terminally double-strep-tagged N-terminal recombinant human FBN2 polypeptide rF86 (Gln29–Asp535).[24] Polyclonal rabbit anti-LTBP2 antiserum (IF: 1:1,000) was raised against the last 254 C-terminal residues of human LTBP2 (Asp1568–Glut1821). Anti-rabbit or -mouse IgG HRP-linked Antibody (#P0399 and #P0260, DAKO GmbH, WB: 1:400) and goat anti-Rabbit IgG Alexa Fluor 555 (#A-21428, Thermo Fisher Scientific, IF: 1:400) were used as secondary antibodies.

Expression constructs

cDNA encoding for full-length human EMILIN1 with NheI/XhoI 5′-/3′-cloning sites was generated by gene synthesis (Genewiz), followed by cloning into a variant of the pCEP-Pu vector.[25] Identified human *EMILIN1* variants were introduced into the obtained construct by site directed mutagenesis using the Q5 Site-Directed Mutagenesis Kit (New England Biolabs).

Dermal fibroblast cell culture

Dermal fibroblasts obtained from skin biopsies from individuals F1:IV-1, F1:IV-2, F4:II-3 (Table 1), a subject with a bi-allelic pathogenic *EFEMP2* (Genbank: NM_016938.5) variant (c.376G>A [p.Glu126Lys]), CL(*EFEMP2*-A), and three age- and sex-matched healthy individuals were cultured in Dulbecco's Modified Eagle Medium (DMEM) (Gibco; Thermo Fisher Scientific) supplemented with 10% fetal bovine serum (PAN-Biotech, Aidenbach), 1% non-essential amino acids (Gibco), 1% penicillin/streptomycin (Gibco), and 0.1% fungizone (Gibco) and incubated at 37°C with 5% CO_2. Primary dermal fibroblasts were isolated from newborn mice.[3] For analysis of ECM network formation, cells were seeded on uncoated glass coverslips at a density of 8×10^4 cells/well in a 24-well plate. For the formation of collagen fibers, the culture medium was supplemented with ascorbate (44 μg/mL L-Ascorbic acid, 130 μg/mL L-Ascorbic acid 2-phosphate sesquimagnesium salt hydrate). For measurement of collagen amounts in cell culture-derived ECM, 5×10^5 human fibroblasts were seeded on a 10 cm dish. Culture medium supplemented with ascorbate was replaced every other day for 9 or 21 days. Transfections of HEK293 cells (adherent epithelial cells of human embryonic kidney/ATCC CRL-1573) were carried out with Lipofectamine (Invitrogen) according to the manufacturer's instructions. HEK293 EBNA cells were cultured on 6-well plates until they reached 80% confluence. For each 1 μg of DNA, 3 μL of FuGENE (Promega) were used.

Immunofluorescence of assembled ECM networks

After culture of 9 days, cells were washed with phosphate-buffered saline (PBS), fixed at −20°C in methanol/acetone, blocked in a PBS/1% bovine serum albumin solution (BSA), and subsequently incubated with primary and secondary antibodies diluted in the blocking solution. Images were obtained from three independent experiments.

Western blot analysis

Cell layers grown on 6-well plates were washed with 1 × PBS before the addition of 200 μL RIPA lysis buffer (Thermo Fisher Scientific) (pre-cooled to 4°C). The protein concentration of each sample was determined using the BCA protein assay (Thermo Fisher Scientific) prior to SDS-PAGE analysis (10%, 12.5%, or 4%–12%) followed by tank blotting onto a nitrocellulose membrane. Ponceau staining (Ponceau S solution, Sigma-Aldrich) was used to visualize the total protein amount. For trichloroacetic acid (TCA) precipitation of cell culture supernatant, 1 volume of 55% TCA was added to 4 volumes of cell culture media.

Determination of TGF-β levels

Total TGF-β levels were measured in conditioned serum-free medium of dermal fibroblast cultures from control subjects and affected individuals collected at day 9 using the Quantikine ELISA kit (#MB100B, R&D Systems) according to manufacturer's instructions. All measurements were obtained from three separate dermal fibroblast culture samples.

Lysyl oxidase activity assay

Cell layers after 9 or 21 days of culture were used to measure total LOX activity using a LOX activity kit (#ab112139, Abcam). The LOX activity assay protocol uses a proprietary LOX substrate that releases hydrogen peroxide after being catalyzed by the presence of LOX in the sample to be analyzed. The amount of released hydrogen peroxide corresponds to LOX activity and is detected using a red fluorescence substrate for HRP-coupled reactions at Ex/Em = 540/590 nm in a fluorescence microplate reader. The assay was performed according to the manufacturer's instruction and was applied on cell layers that were seeded and collected as described above.

Table 1. Overview of *EMILIN1* genotypes and clinical characteristics

Family	**1**	**1**	**2**	**2**	**3**	**4**	**Number and % affected individuals**
Proband	**F1:IV-1**	**F1:IV-2**	**F2:IV-2**	**F2:IV-3**	**F3:III-1**	**F4:II-3**	
Demographic features							
Age at last evaluation	7 y	5 y	3 mo	2 we	6 mo	18 mo	mean 2.33 years (range 2 we–7 y)
Sex	M	M	M	M	M	M	100% male
Parental consanguinity	+	+	+	+	–	–	4/6 (67%)
Ethnicity	Middle-Eastern	Middle-Eastern	Middle-Eastern	Middle-Eastern	European white	Hispanic American	not applicable
Clinical characteristics							
Craniofacial features							
Short palpebral fissures	+	+	–	–	+	–	3/6 (50%)
Downslanted palpebral fissures	+	+	–	–	–	–	2/6 (33%)
Epicanthus	+	+	–	unknown	–	–	2/5 (40%)
Blue sclerae	+	+	–	unknown	+	–	3/5 (60%)
Convex nasal ridge	+	+	–	unknown	+	–	3/5 (60%)
Wide nasal ridge	+	+	–	unknown	+	–	3/5 (60%)
Thin upper lip	+	+	–	+	+	–	4/6 (67%)
Flat philtrum	+	+	–	–	+	–	3/6 (50%)
Highly arched palate	+	+	–	unknown	+	–	3/5 (60%)
Dolichocephaly	+	+	–	+	–	–	3/6 (50%)
Cardiovascular features							
Aortic tortuosity	+	+	+	+	+	+	6/6 (100%)
Tortuosity of other arteries	+	unknown	+	+	+	+	5/5 (100%)
Aortic root dilatation	+	–	–	+	+	+	4/6 (67%)
Coarctation of the aorta	–	–	+	+	–	–	2/6 (33%)
Arterial stenosis	–	–	+	+	–	–	2/6 (33%)
Abnormal implantation of aortic branches	–	–	+	–	+	–	2/6 (33%)
Arterial dissection	–	–	–	–	–	–	0/6 (0%)
Musculoskeletal features							
Joint hyperlaxity	+	+	–	+	–	–	3/6 (50%)

(*Continued on next page*)

Table 1. ***Continued***

Family	**1**	**1**	**2**	**2**	**3**	**4**	**Number and % affected individuals**
Proband	**F1:IV-1**	**F1:IV-2**	**F2:IV-2**	**F2:IV-3**	**F3:III-1**	**F4:II-3**	
Fractures	–	+	+	+	+	+	5/6 (83%)
Number of fractures	not applicable	4	7	1	2	1	mean 3
Age at fracturing	not applicable	neonatal, 4 y	6 we	birth	birth	8 mo	N/A
Muscle hypotonia	–	–	–	+	+	–	2/6 (33%)
Additional features							
Cutis laxa	+	+	–	–	+	–	3/6 (50%)
Thin, velvety skin	+	+	–	unknown	+	–	3/5 (60%)
Petechiae at birth	–	–	–	+	+	–	2/6 (33%)
Cephalohematoma	+	–	–	+	+	–	
Respiratory distress	–	–	+	+	+	–	3/6 (50%)
Hydronephrosis	+	–	+	+	–	+ (resolved)	4/6 (67%)
Seizures	–	+	–	–	+	–	2/6 (33%)
Molecular characteristics							
cDNA change	c.831dup	c.831dup	c.151del	c.151del	c.119dup, c.2457_2482dup	c.1606C>T	
Protein change	p.Ala278Serfs*11	p.Ala278Serfs*11	p.Arg51Glyfs*14	p.Arg51Glyfs*14	p.Ser40Argfs*34, p.Gln828Leufs*59	p.Gln536*	
Zygosity	homozygous	homozygous	homozygous	homozygous	compound heterozygous	homozygous	

Abbreviations: y, year; mo, months; we, weeks; M, male; +, present; -, absent.

Mass spectrometry analysis

For the identification of altered protein levels between F1:IV-I and ctrl1 dermal fibroblasts, supernatants and cell lysates after 4 days of culture were subjected to mass spectrometry analysis. All samples were precipitated by addition of acetone and reduced with 10 mM DTT in 50 mM NH_4HCO_3 at 56°C for 45 min. The reduced cysteine residues were alkylated with 50 mM iodoacetamide in 50 mM NH_4HCO_3 for 30 min in the dark. Protein pellets were then rehydrated in ice-cold trypsin solution in 10 mM NH_4HCO_3 (10 ng/μL trypsin, "sequencing grade," Promega). After 45 min on ice, the trypsin solution was exchanged for the digestion buffer solution and the proteins were digested at 37°C overnight. The digestion was stopped by addition of 20 μL of 10% formic acid and subsequent incubation for 30 min at 37°C. Liquid chromatography mass spectrometry measurement (LC-MS) was performed with the HCT ETD II ion trap mass spectrometer equipped with a nano ESI ionization source (Bruker Daltonics). Data collection for the MS and Tandem MS (MS/MS) spectra was performed with Compass 3.0 software (Bruker). The protein identification was carried out by searching the SWISSPROT database with the program MASCOT 2.2 (Matrix Science Ltd).

Quantitative real-time PCR

Cells were seeded in 24-well plates at 8×10^4 cells/well and grown for 9 days. Total RNA was prepared by using the Trizol reagent (Invitrogen) following the manufacturer's protocol. RNA (0.5 μg/sample) was reverse transcribed using the Biorad iScript cDNA synthesis kit (Bio-Rad). Triplicate samples were amplified using the SensiFAST SYBR Hi-ROX Kit (Bioline GmbH) in a StepOnePlus Real-Time PCR Detection System (Applied Biosystems). Data analysis was performed using the extended delta CT-method using an averaged CT-value derived from two reference genes.[26] *GAPDH* and ribosomal protein lateral stalk subunit P0 (*RPLP0*) were used as reference genes. Used primers are listed in Table S2.

Sequential skin extraction

Mouse skin samples were ground in liquid nitrogen and each 1 mg of powderized tissue was subsequently incubated with 50 μL of extraction buffer I (0.05 M Trizma base [pH 7.4], 0.15 M NaCl [Sigma-Aldrich]), buffer II (buffer I [pH 7.4], 0.01 M EDTA), buffer III (buffer I [pH 7.4], 0.01 M EDTA, 2 M Urea), and buffer IV (buffer I [pH 7.4], 0.01 M EDTA, 8M Urea) overnight at 4°C. After each incubation step, samples were centrifuged at full speed for 15 min at 4°C and supernatants were collected as fraction I, II, III, and IV for buffer I, II, III, and IV, respectively. Each buffer was freshly supplied with Protease Inhibitor Cocktail solution (50×) (Sigma-Aldrich) at a 1:50 dilution. After TCA precipitation, aliquots of each fraction were separated by electrophoresis onto 4%–12% gradient SDS polyacrylamide gels and analyzed by western blot.

Transmission electron microscopy

Preparation of human skin biopsies for TEM analysis was as previously described.[25,27] 3 mm skin biopsies from individuals F1:IV-1 and F3:III-1, two subjects with bi-allelic pathogenic *EFEMP2* variants (c.608A>C [p.Asp203Ala])—CL(*EFEMP2*-B) and CL(*EFEMP2*-C), respectively—and two age-matched control subjects were initially immersed in a fixative solution of 4% glutaraldehyde for transport.

For transmission EM analysis of mouse *Emilin1*$^{-/-}$ skin, skin biopsies were harvested and fixed in cacodylate buffer. Contrasting was carried out by addition of 1.5% aqueous uranyl acetate solution for 15 min at 37°C followed by a washing step in distilled water for 4 min in lead nitrate. After incubation with 2% osmium (VIII) oxide for 2 h in the dark at RT, dehydrogenation and embedding in propylene oxide took place. Ultra-thin sections with a thickness of 70 nm were applied to carbon nanotubes coated with carbon-reinforced plastic film. EM images were taken with a JEM-2100 PLUS transmission electron microscope (JEOL Ltd.).

Collagen fibers produced by dermal fibroblasts in cell culture were visualized by negative staining and TEM.[28] For negative staining, cell culture supernatant was directly used without further treatment and stained with uranyl formate at pH 4.2–4.5. Specimens were examined in a Philips/FEICM 100 BioTWIN transmission electron microscope operated at 60 kV accelerating voltage, or in a Tecnai G2 Spirit transmission electron microscope, operated at 80 kV (FEI company). Images were recorded with a side-mounted Olympus Veleta camera with a resolution of 2,048 × 2,048 pixels (2k × 2k) and the ITEM acquisitions software (Olympus Life Science).

Immunoelectron microscopy

Skin biopsies from F4:II-2, and F4:II-3 were labeled using *en bloc* diffusion of primary antibodies[27] followed by the appropriate secondary anti-rabbit, anti-guinea pig, or anti-rat IgG conjugated with 1-, 5-, or 10-nm gold particles. The 1-nm gold was subsequently enhanced with additional gold precipitation followed by standard fixation and embedding for transmission electron microscopy. Used antibodies were polyclonal rabbit anti-EMILIN1[3] and monoclonal anti-EFEMP2 (mab347).[22]

Collagen quantification

For collagen fibril quantification, the cross-sectional area was measured using ImageJ Fiji.[29] 600 collagen fibrils (150 fibrils of four independent fields of view) were analyzed for subjects F1:IV-1 and F3:III-1, two subjects with *EFEMP2* pathogenic variants, and two age- and sex-matched control subjects, respectively. The circumference of each area of measured fibrils was manually measured three times, and the means of these measurements were used for further calculations. Spatial calibration for diameter measurements were applied in each sample against the scale bar. Differences in mean and distribution were analyzed in GraphPad Prism 5, using respectively an unpaired t test and Mann-Whitney test when comparing two groups, and one-way ANOVA and Kruskal-Wallis test when comparing more. For all analyses, the null hypothesis was rejected at the 0.05 level of significance.

Collagen protein quantification and crosslinking analysis

To measure the collagen crosslinks in mouse skin, equal sizes of skin were punched out of the shaved back skin of each mouse using a 6 mm-Ø biopsy punch, rinsed with 1× PBS, and stored at −80°C. For crosslink analysis, samples (about 20 mg wet weight) were reduced by sodium borohydride to stabilize acid-labile collagen crosslinks (Sigma-Aldrich; 25 mg $NaBH_4$/mL in 0.05 M NaH_2PO_4/0.15 M NaCl [pH 7.4], 1 h on ice, 1.5 h at room temperature). Specimens were digested two times with "high purity bacterial collagenase" (Sigma-Aldrich; 50 U/mL, 37°C, 18 h). After centrifugation, the soluble fractions (collagen crosslinks) were hydrolyzed in 6 N HCl at 110°C for 24 h. The hydrolysates were precleaned by solid phase extraction (Agilent). Dried eluates were dissolved in sodium citrate buffer (pH 2.2) and analyzed on an amino

acid analyzer (Biochrom 30+, Biochrom) in a three-buffer gradient method and post-column ninhydrin derivatization. Elution took place for 5 min (flow rate: 15 mL/h) with sodium citrate buffer (pH 4.25), 40 min with sodium citrate buffer (pH 5.35), and 20 min with sodium citrate/borate buffer (pH 8.6) at 80°C. Quantification was based on ninhydrin generated leucine equivalence factors (DHLNL, HLNL: 1.8; HP: 1.7; HHMD: 3.4).[30] The nomenclature used in this manuscript refers to the reduced variants of crosslinks (DHLNL, dihydroxylysinonorleucine; HLNL, hydroxylysinonorleucine; HHMD, histidinohydroxymerodesmosine). The determination of the amount of collagen and protein was carried out on the hydrolyzed samples before subjection to the solid-phase extraction. The collagen content was calculated on the basis of 14 mg hydroxyproline per 100 mg collagen.

Histology and immunohistochemistry

Histology and immunohistochemistry were performed on paraffin-embedded aortic tissue samples of F2:IV-2, CL(*EFEMP2*-D) (c.835C>T [p.Arg279Cys]; c.1070_1073dupCCGC [p.Asp359Argfs*2] variants), and an age-matched control subject. The control sample was obtained from an individual with suspected vascular Ehlers-Danlos syndrome but with no pathogenic variants detected by *COL3A1* sequencing and normal elastic fibers and collagen on orcein staining. Paraffin-embedded samples were cut to 5-μm-thick samples, deparaffinized, and rinsed in distilled water. Weigert's Resorcin-Fuchsin, Verhoeff-Von Gieson, and Trichrome-Masson staining were performed as previously described.[25,31] Hematoxylin-eosin and Verhoeff-Von Gieson staining was performed in diagnostic setting on aortic tissue of F2:IV-2, solely (Figure S3). For immunohistochemistry, epitope unmasking was performed with citrate buffer (10 mM [pH 6]).[31] All sections were visualized with a Zeiss Axio Observer Z1 microscope.

Micro-CT analysis

Femur structural properties were evaluated using a high-resolution micro-CT scanner (μCT 35; Scanco Medical AG) as described previously.[32,33] Isolated left femora from perinatal (P4), juvenile (8 weeks), and adult (14 weeks of age) *Emilin1*$^{-/-}$ and wild-type littermate control mice were stored in 70% EtOH in 1.5 mL tubes at 4°C until micro-CT analysis. Femora of juvenile and adult mice were scanned at a voxel size of 7 × 7 × 7 μm, 70-kVp tube voltage, 114-mA tube current, and 400-ms integration time. For separation of cortical and trabecular bone signals, threshold segmentation was performed. For trabecular bone extraction, data were globally thresholded with 23%, and for cortical bone extraction a threshold of 29% was applied. 143 slices (1 mm) were evaluated in the distal femur with the volume of interest 1 mm below the growth plate (secondary spongiosa) to analyze trabecular bone. For assessment of cortical bone, 107 slices (0.75 mm) were evaluated at the femoral midshaft. Trabecular parameters included bone volume (mm^3), tissue volume (mm^3), bone volume fraction (%), trabecular separation (mm), trabecular thickness (mm), trabecular number (1/mm), and connectivity density ($1/mm^3$). At the diaphysis, tissue area (mm^2), cortical area (mm^2), marrow area (mm^2), and cortical thickness (mm) were determined. Bone mineral density (BMD) of juvenile and adult murine femora was determined at the level of metaphysis and diaphysis.

The femora of the perinatal mice were scanned at a voxel size of 3.5 × 3.5 × 3.5 μm, 45-kVp tube voltage, 177-μA tube current, and 400-ms integration time. For the analysis, the total length of the calcified primary ossification center (POC) was determined. BMD was then calculated at midshaft using a threshold of 36%. The volume of interest (VOI) covered 20% of the total length.

Mechanical testing

Left femora from adult (14 weeks of age) *Emilin1*$^{-/-}$ and wild-type littermate control mice were wrapped in saline-soaked gauze in 1.5 mL tubes and stored at −20°C until mechanical testing. Femora were loaded until failure by a three-point bending test using a material testing machine (Z2.5/TN1S, Zwick GmbH & Co.) as previously described.[34] Briefly, femora were loaded at mid-diaphysis in anterior-posterior direction using a 100-N load cell. The distance between support points, 1.5 mm in diameter, was 5 mm. After preloading at 0.1 N, 0.05 mm/s, a loading rate of 1 mm/min was applied perpendicularly to the long axis of the bones. Ultimate load (N), deformation (mm), energy (mJ), and stiffness (N/mm) were determined from the load-deformation curve. Ultimate stress (MPa) and ultimate strain (%), energy density (mJ/mm^3), as well as elastic modulus (MPa) were calculated based on the area moment of inertia obtained from micro-CT measurements.

Statistical analysis

All values are presented as means ± standard deviation (SD). Two-tailed unpaired t test with Welch's correction was used for statistical analysis to compare two groups. p values smaller than 0.05 were considered as statistically significant. Statistical differences among more than two groups were determined by ANOVA (analysis of variance) and subsequent Bonferroni multiple comparison post-tests.

Results

Bi-allelic *EMILIN1* loss-of-function variants cause arterial tortuosity, aortic aneurysms, and transient osteopenia

Table 1 and Figure 1 summarize and illustrate the relevant clinical features in six affected subjects from four unrelated families. Extensive case reports and a summary of all evaluated clinical features can be consulted in the supplemental notes and Table S1. The parents of the affected individuals of family 1 and 2 are consanguineous. All affected individuals presented with generalized arterial tortuosity and fractures. In three individuals, prenatal ultrasound showed arterial tortuosity (F2:IV-3), a suspicion for aortic coarctation (F4:II-3), and/or renal hydronephrosis (F1:IV-1, F2-IV-2, and F2:IV-3). At birth, anthropometric parameters were within normal ranges. F2:IV-2 and F2:IV-3 presented with neonatal respiratory distress and F3:III-1 had episodes of apnea.

Five out of six individuals presented with fractures of the ribs, clavicle, acromion, metatarsal, or long bones such as the radius, ulna, and fibula (F1:IV-2, F2:IV-2, F2:IV-3, F3:III-1, F4:II-3). In addition, individuals F2:IV-3 and F3:III-1 had bilateral parietal bone fractures underlying a cephalohematoma. All fractures were detected prenatally or during the first weeks of life and fracture risk likely diminished with age as only one subject suffered from a traumatic fracture at the age of 4. Accordingly, bone densitometry at 6 weeks of age showed osteopenia in subject

F2:IV-2 but was normal in both siblings of family 1 at ages 7 and 5, respectively.

Arterial tortuosity was present in all individuals, mainly affecting the aorta and main aortic side branches, including the carotid, pulmonary, and brachiocephalic arteries. In family 1, both siblings displayed tortuous retinal arteries. Four subjects developed an aneurysm of the aortic root with an age at diagnosis ranging from birth (F2:IV-3: Z-score 7.49), to ages 1 (F3:III-1; Z-score 3.4, F4:II-3; Z-score 6.62) and 7 (F1:IV-1; Z-score 4.78), respectively. The aortic aneurysm in F2:IV-3 extended to the entire aortic arch, descending aorta, and intrathoracic segments of the left carotid arteries and left subclavian arteries. In F4:II-3, Z-scores progressively increased to +6.62 SD and +10.92 SD, respectively, at the level of the aortic root and ascending aorta, at the age of 13 months. At the age of 18 months, he underwent a valve sparing aortic root, ascending and hemi arch replacement. Aortic coarctation was found at birth in both siblings of family 2 and F3:III-1. Additional vascular stenoses were located at the pulmonary (F2:IV-2, F3:III-1), carotid (F2:IV-3), or subclavian (F2:IV-2, F2:IV-3) arteries. Thus far, no arterial dissections occurred. Subjects F1:IV-2 and F4:II-3 showed mild aortic valve regurgitation. Subject F4:II-3 was diagnosed with an ostium secundum atrial septal defect with dilated right atrium and right ventricular hypertrophy. A common brachiocephalic trunk and aberrant implantation of the right subclavian artery was reported in individual (F2:IV-2), who later developed progressive thoracic and abdominal aortopathy requiring two surgical repairs of the stenotic aortic regions. At 3 months of age, he showed refractory hypertension and severe left ventricular hypertrophy and eventually died from post-operative complications.

Most affected individuals showed craniofacial abnormalities with short and downslanted palpebral fissures, epicanthus, a convex and/or wide nasal ridge, prominent nasolabial folds and sagging cheeks, a long philtrum, thin upper lip, micrognathia, and a high arched palate. Connective tissue features included blue sclerae (F1:IV-1, F1:IV-2, and F3:III-1), mild CL and a thin and velvety skin (F1:IV-1 F1:IV-2, and F3:III-1), joint hyperlaxity (F1:IV-1 F1:IV-2, and F2:IV-3), and arachnodactyly (F1:IV-1). Individual F1:IV-1 presented with right inguinal hernia, which was surgically corrected. Of note, two subjects (F2:IV-3 and F3:III-1) presented with diffuse cutaneous petechiae at birth. Individual F4:II-3 presented with a small anterior fontanel.

Neuromotor development was reportedly normal in all assessable individuals. Afebrile seizures occurred during the first year of life in subject F1:IV-2 and in the context of the extradural hemorrhage following bilateral parietal bone fracture in F3:III-1. In family 2, MRI showed hypoplasia of the corpus callosum with a globally diminished supratentorial white matter volume with an enlarged extradural space in the elder and bilateral microbleeds in the younger sibling. Muscular hypotonia was noted upon clinical examination in F2:IV-3 and F3:II-3. Subject F4:II-3 presented with increased muscle tone in the hands.

Urological manifestations were observed in three out of four families, including hydronephrosis (F1:IV-1, F2:IV-2, F2:IV-3, and F4:II-3) (congenital and transient) and duplication of the renal collecting system (F2:IV-3).

Exome sequencing (ES) identified bi-allelic loss-of-function variants in *EMILIN1* (Genbank: NM_007046.4) in all affected individuals (Figure 1). The first two families harbor homozygous frameshift variants in *EMILIN1,* c.831dup (p.Ala278Serfs*11) and c.151del (p.Arg51 Glyfs*14), respectively. In the third family, the proband harbored compound heterozygous variants (c.119dup [p.Ser40Argfs*34], maternally inherited) and a 25 base pair duplication (c.2457_2482dup [p.Gln828Leufs*59], paternally inherited). In the fourth family, the proband has a homozygous nonsense variant c.1606C>T (p.Gln536*). All variants segregate in family members according to disease and carrier status. All variants are absent in population databases. Prior to ES, SNP-microarray in F2:IV-2 revealed a 47,XXY karyotype indicating Klinefelter syndrome.

Homozygous frameshift pathogenic variants in *EMILIN1* severely impair protein production

The premature stop codon *EMILIN1* variants in family 1 and 4 are predicted to induce nonsense-mediated decay (NMD)[35] (Figures 1E and S1). Dermal fibroblasts from F1:IV-1, F1:IV-2, and F4:II-3 show a significant reduction of *EMILIN1* mRNA levels compared to age- and sex-matched control subjects (Figure S2A). We then transfected HEK293 cells with a full-length *EMILIN1* expression construct containing the c.831dup frameshift variant. Western blot using a monoclonal antibody recognizing an N-terminal epitope cannot detect full-length EMILIN1 (Figure 2A). However, a truncated EMILIN1-positive band at around 25 kDa (the expected amino acid sequence is depicted in Figure S1) is detectable in cell lysates but is barely present in the supernatant (Figure 2A). In accordance, western blot analysis of F1:IV-1 and F1:IV-2 fibroblast cells reveals only a faint band of truncated EMILIN1 at around 32 kDa in lysates, but not in the supernatants (Figure 2B). Similarly, a p.Gln536* pathogenic variant strongly abolishes EMILIN1 production in skin fibroblasts isolated from F4:II-3, though a minor amount of full-length EMILIN1 remains detectable in the cell lysate (Figure S2B). Consequently, EMILIN1 is absent in ECM networks assembled by F1:IV-1, F1:IV-2, and F4:II-3 cells (Figure 2C) upon immunofluorescence staining. However, immunogold labeling of extracellular fibers with EMILIN1 antibody reveals that EMILIN1 is still deposited in a very small quantity in the ECM of F4:II-3 cultured fibroblasts (Figure S2C). Of note, we observed a faint band in control fibroblasts around 28 kDa, a lower molecular weight compared to the truncated mutant protein in fibroblasts of affected individuals of family 1. The composition and function of this protein remains to be established. Nevertheless, the

band was absent in fibroblasts of affected individuals of family 1.

EMILIN1 deficiency affects elastic fiber integrity

We performed histology in tissue of the descending aorta from individual F2:IV-2, an individual with compound heterozygous *EFEMP2* pathogenic variants, CL(*EFEMP2*-D), and an age-matched control subject (Figure 3A). In addition, we evaluated end-stage diseased aortic samples of the individuals with *EMILIN1* and *EFEMP2* pathogenic variants, i.e., aortic coarctation and dissection, respectively. Weigert's Resorcin-Fuchin staining reveals highly disorganized, thinner, and irregular elastic lamellae in aortic tissue from both F2:IV-2 and CL (*EFEMP2*-D). This is even more pronounced in end-stage vascular tissue with severe elastic fiber fragmentation and fibrosis. Verhoeff-Von Gieson staining performed in a diagnostic context highlights the severe medial degenerative changes and mild intimal fibrosis with fragmentation of the elastic lamellae (Figure S3).

At the ultrastructural level, transmission electron microscopy (TEM) analysis in control dermal biopsies shows elastic fibers with a solid, dense core of elastin surrounded by a sparse mantle of microfibrils (Figure 3B). In contrast, elastic fibers in the skin of F1:IV-1, F3:III-1, and F4:II-3 show a fragmented elastin core with microfibrils present in the intermediate space, resembling the ultrastructural elastic fiber abnormalities in the dermis of both subjects with *EFEMP2* pathogenic variants, CL(*EFEMP2*-B) and CL(*EFEMP2*-C). Immunogold labeling TEM with a specific antibody against EMILIN1 in skin from F4:II-3 shows an almost complete absence of EMILIN1-positive signals from elastic fibers compared to family members carrying only one mutant allele (Figure 3C). Also, immunogold labeling of F4:II-3 cultures confirms the presence of EMILIN1 in minor amounts (Figure S2C).

Loss of EMILIN1 severely impacts EFEMP2 ECM deposition

EMILIN1 directly interacts with EFEMP2 and is required for its linear matrix deposition.[5] Similar to EFEMP2-deficient fibroblasts, EMILIN1-deficient fibroblasts from the affected individuals of family 1 show strongly reduced EFEMP2 fibers, but normal fibronectin, FBN1, FBN2, LTBP1, and LTBP2 deposition (Figures 4A, 4B, and S4). However, absence of EFEMP2 does not appear to affect EMILIN1 ECM deposition in EFEMP2-deficient fibroblasts (Figure 2C). Furthermore, western blot analysis shows normal amounts of secreted EFEMP2 by F1:IV-1, F1:IV-2, and F4:II-3 cells (Figure S5). Therefore, our data indicate that EFEMP2 ECM deposition specifically requires EMILIN1. Immunogold labeling confirms that EFEMP2 is nearly absent in F4:II-3 skin elastic fibers but is present in unaffected parents and siblings (Figure 4C).

Loss of EMILIN1 affects LOX function

EFEMP2 is a known binding partner of LOX, a copper-containing enzyme that catalyzes the covalent crosslinking of elastin and collagen and plays a pivotal role in the activation of LOX.[16,36] We investigated whether LOX abundance and activity is affected in EMILIN1-deficient and EFEMP2-deficient fibroblast cultures. Mass spectrometry analysis of F1:IV-1 fibroblast culture supernatant indicates a significant reduction in LOX levels (Figure S6A). Also, LOX transcript levels are significantly reduced in all analyzed *EMILIN1* mutant fibroblasts (Figure S6B), while FN1 transcript levels remain unaltered (Figure S6C). Western blot analyses confirm a strong reduction of total LOX in the supernatants of cultured F1:IV-1, F1:IV-2, and F4:II-3 fibroblasts (Figure 5A). Furthermore, either EMILIN1 or EFEMP2 deficiency cause similarly diminished active LOX levels in cell culture supernatants of F1:IV-1, F1:IV-2, F4:II-3, and CL(*EFEMP2*-A) cells (Figure 5A). Interestingly, quantitation of intensities of processed and unprocessed proLOX western blot signals reveals that the percentage of processed LOX of total LOX was similarly reduced by about 50% for EMILIN1-deficient F1:IV-1, F1:IV-2, and F4:II-3 and EFEMP2-deficient CL(*EFEMP2*-A) fibroblasts (Figure S6C). Furthermore, LOX enzymatic activity is significantly reduced by 35%–70% in F1:IV-1, F1:IV-2, F4:II-3, and CL(*EFEMP2*-A) cells (Figures 5B and S6E).

EMILIN1 deficiency affects collagen network assembly and crosslinking

We next investigated collagen fiber assembly. Hydroxyproline content in long-term culture of F1:IV-2 cells indicates about 50% reduction in total collagen deposition (Figure S6F). Immunofluorescence staining revealed that F1:IV-1, F1:IV-2, F4:II-3, and CL(*EFEMP2*-A) cells produce very thin collagen I fibers at low density (Figure 5C). Negative staining transmission electron microscopy (TEM) of EMILIN1-deficient F1:IV-1, F1:IV-2, F4:II-3 as well as EFEMP2-deficient CL(*EFEMP2*-A) fibroblasts show a thin and curly appearance of collagen fibrils displaying a less distinct cross-band pattern (Figure 5D).

Emilin1$^{-/-}$ mice recapitulate deficient EFEMP2 and collagen deposition

In murine *Emilin1*$^{-/-}$ dermal fibroblasts EFEMP2 fiber formation is strongly reduced, while other elastic fiber networks appear non-affected (Figure S7). Dermal fibroblast cultures show thin and curly collagen fibrils similar to human cell cultures (Figure 5E). Western blot analysis of *Emilin1*$^{-/-}$ skin extracts show more extractable EFEMP2 and collagen I compared to wild-type control subjects for all used elution buffers with different protein extraction strength suggesting reduced LOX-mediated crosslinking and deficient anchorage of both proteins within the ECM (Figure S8). Crosslink analysis of *Emilin1*$^{-/-}$ skin confirms a significant reduction of collagen crosslinks (Figure 5F).

EMILIN1 deficiency affects collagen synthesis and TGF-β activity

Cell lysates from EMILIN1-deficient F1:IV-1, F1:IV-2, and F4:II-3 fibroblast cultures show significantly increased

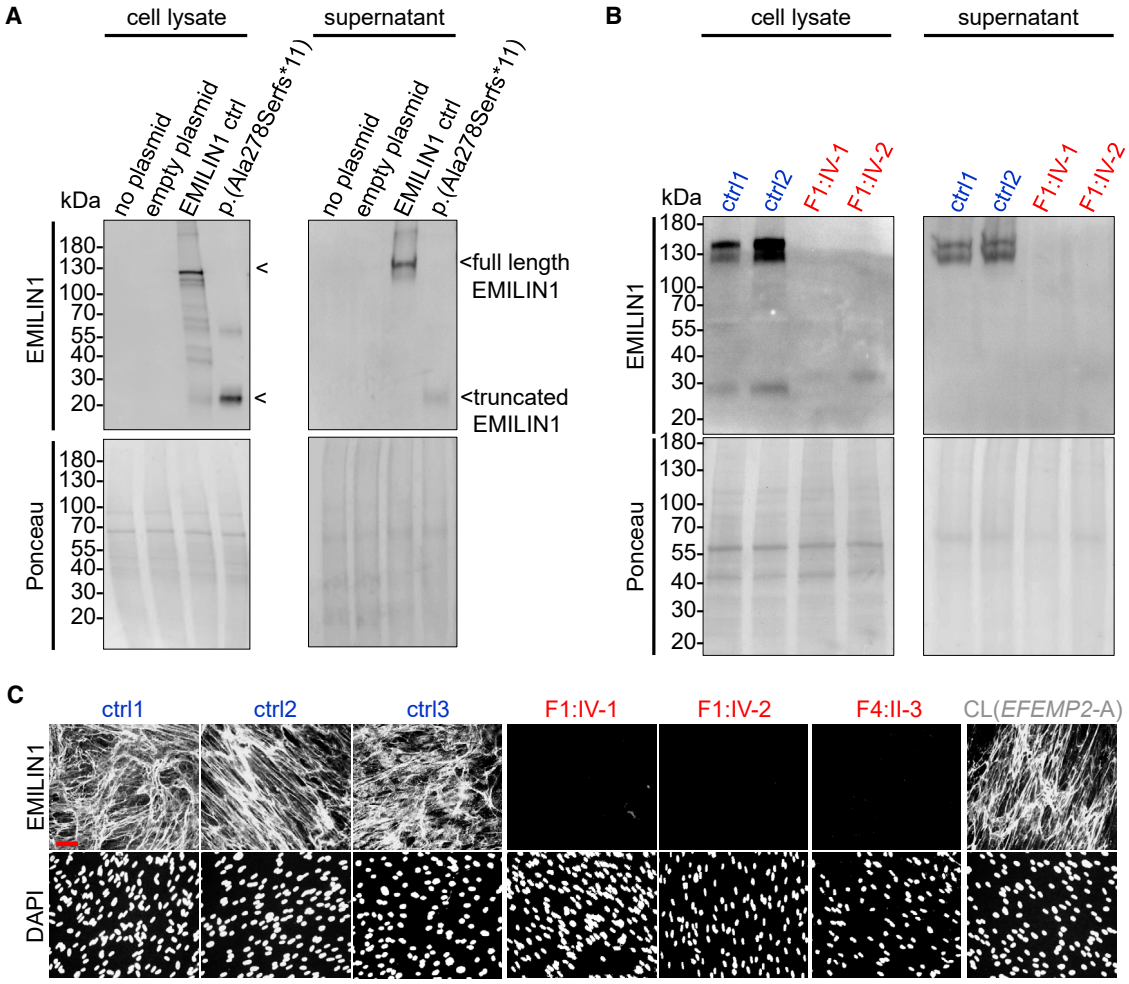

Figure 2. Bi-allelic pathogenic variants in *EMILIN1* lead to loss of mRNA and protein production

(A) Abolishment of protein production shown by introducing the p.Ala278Serfs*11 *EMILIN1* variant into a human EMILIN1 full-length overexpression construct. Secreted amounts of truncated EMILIN1 by HEK293 cells transfected with the p.Ala278Serfs*11 construct were hardly detectable.

(B) Western blot analyses of cell lysates and supernatants from F1:IV-1 and F1:IV-2 fibroblasts show complete abolishment of secreted EMILIN1.

(C) Immunofluorescence analyses of F1:IV-1, F1:IV-2, and F4:II-3 fibroblast cultures indicate absence of EMILIN1 within assembled ECM networks. EMILIN1-positive fibers are detected in age-matched healthy controls and in fibroblast cultures derived from an individual with CL carrying a homozygous EFEMP2 pathogenic variant (CL(*EFEMP2*-A)). Scale bar, 50 μm.

collagen I synthesis (Figure 6A). Also qPCR analyses indicate increased transcripts levels of collagen chains in F1:IV-1, F1:IV-2 cells, and elevated protein levels are detected by mass spectrometry analysis of cell culture supernatants (Figures 6A and S9B). In congruence, cartilage oligomeric matrix protein (COMP), a known collagen chaperone,[37] is increased in the supernatant of EMILIN1-deficient cell cultures (Figure S9C). Since EMILIN1 is known as negative regulator of TGF-β activity,[8] we analyzed transcript levels of known TGF-β response elements. Total levels of secreted TGF-β are normal in F1:IV-1 and F1:IV-2 cells (Figure S9A), but F1:IV-2 fibroblasts show significantly increased transcription of *PAI1* and *CTGF* and F1:IV-1 cells show increased *COL3A1* transcription (Figure 6B). In aortic wall tissue of F2:IV-2 and CL(*EFEMP2*-A), phospho-SMAD2 staining is not clearly augmented. However, CTGF staining (Figure 6C) and collagen deposition seems increased (Figure 6D). Collagen deposition shows either a diffuse, loosely packed or a bulky appearance, thickening the intralaminar spaces, similar to the collagen distribution within the aortic wall of CL(*EFEMP2*-D) (Figure 6D). In line with this finding and previously reported data,[6] immunofluorescence shows increased collagen I signals and an abnormal distribution within the aortic wall of *Emilin1*$^{-/-}$ mice (Figure S10). Overall, though TGF-β signaling could be increased in initial stages of extracellular matrix assemble, this cannot be confirmed in end-stage diseased vascular samples.

EMILIN1 deficiency affects collagen fibril formation

TEM of dermal biopsies of individuals F1:IV-1 and F3:III-1 show highly variable collagen fibril size (Figure 7A). Quantification confirms a wider distribution shifted toward

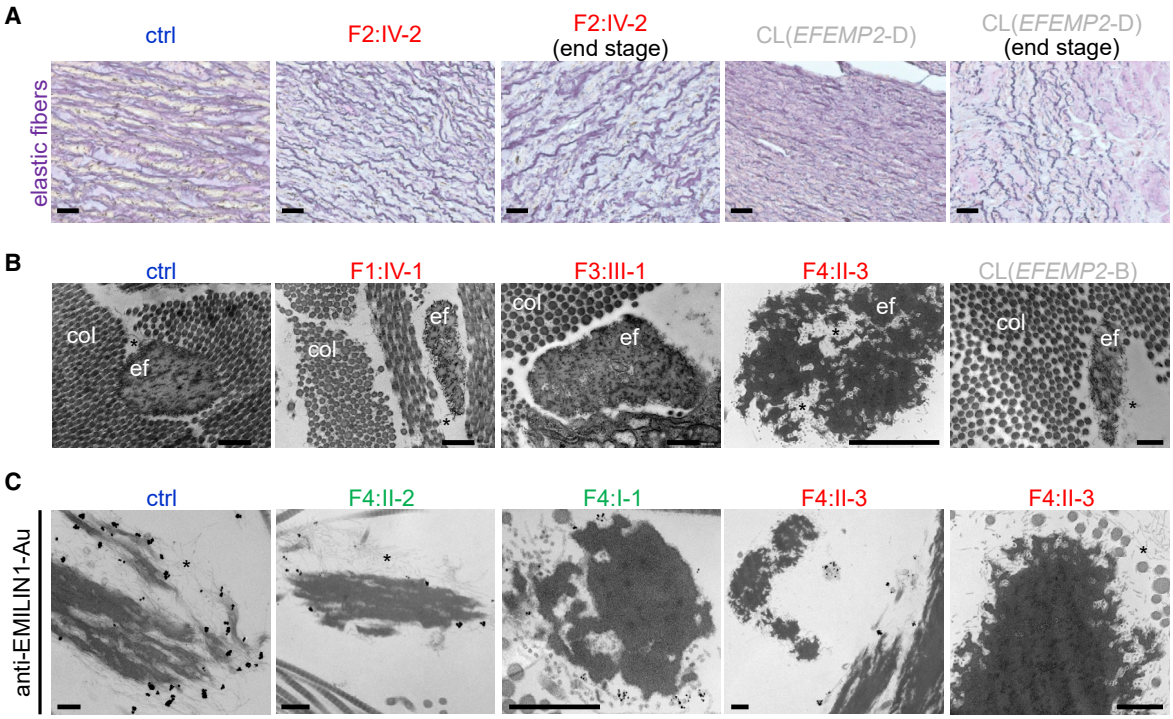

Figure 3. EMILIN1 deficiency affects elastic fiber integrity

(A) Severe disorganization and fragmentation of elastic fibers in aortic media from F2:IV-2 and an individual with CL carrying a bi-allelic EFEMP2 pathogenic variant (CL(*EFEMP2*-D)) as detected by Weigert's Resorcin-Fuchsin staining. All obtained sections are matched to their anatomical locations (descending aorta). Reduced presence of intact elastic fibers is even more pronounced in end-stage vascular tissue. Scale bar, 25 μm.

(B) Representative micrographs from TEM analysis of dermis from F1:IV-1, F3:III-1, F4:II-3, and CL(*EFEMP2*-B) skin biopsies (images of CL(*EFEMP2*-C) not shown) showing an abnormal ultrastructure of elastic fibers (ef) in cross section indicated by a fragmented elastin core and a bare mantle of microfibrils (indicated by asterisk where visible). The presence of collagen fibrils (col) in cross section is indicated. Elastin shows variability in staining intensity due to slight changes in fixation protocols used at the two different imaging centers. Scale bars, 500 nm.

(C) TEM analysis after immunogold labeling of EMILIN1 in skin biopsies from F4:II-3 shows reduced presence of EMILIN1 within the elastic fiber/microfibril network in comparison to unaffected sibling (F4:II-2) or parent (F4:I-1). Scale bars, 200 nm. Font legend: red, affected individual; green, non-affected carrier; blue, control subject.

larger diameters (91.9 ± 6.9 nm versus 77.0 ± 3.4 nm in control dermis; $p < 0.0001$) (Figure 7B). Similar variability of collagen fibril size is present in the dermis of both individuals with *EFEMP2*-related cutis laxa (CL(*EFEMP2*-B) and CL(*EFEMP2*-C)) (90.9 ± 5.6 nm; $p < 0.0001$ compared to control dermis) (Figure 7B). In accordance, collagen fibers in murine *Emilin1*$^{-/-}$ skin at 3 months of age display an irregular morphology and larger diameters (79 ± 10.8 nm in wild-type versus 121.1 ± 28.3 nm in *Emilin1*$^{-/-}$; $p < 0.0001$) (Figures 7C and 7D). Moreover, the EFEMP2- and EMILIN1-deficient samples show a smoother surface with less small perpendicular protrusions from the fiber. Longitudinal sections of collagen fibrils indicate variability of the diameter along the fibril axis (Figure 7C). No significant changes in area occupied by fibrils or by interfibrillar connective tissue are observed in dermal biopsies from F1:IV-1, F3:III-1, or murine *Emilin1*$^{-/-}$ skin, while significant alterations are present in CL(*EFEMP2*) skin (occupied area: 45.4% ± 4.8% control versus 52.3% ± 9.9% CL(*EFEMP2*), $p < 0.01$; interfibrillar space: 52.2% ± 5.0% control versus 45.0% ± 3.5% CL(*EFEMP2*), $p < 0.01$) (Figure S11).

EMILIN1 is required for proper bone structure in mice

Bone fractures are key clinical features in individuals with *EMILIN1* pathogenic variants (Figure 1C, Table S1). We performed micro-CT analysis of isolated femora from juvenile and adult *Emilin1*$^{-/-}$ mice as well as wild-type controls. Representative micro-CT images near the distal femoral metaphyseal region and a cross-sectional view of distal adult *Emilin1*$^{-/-}$ femora exhibit decreased trabecular bone (Figure 8A). However, femur length (Figure S12B) and bone mineral density are not significantly different in juvenile or adult *Emilin1*$^{-/-}$ femora compared to wild-type controls (Figure S12C). Also, at the level of the metaphysis, bone volume, bone connectivity density, and trabecular thickness show no significant alteration (Figure S12D). Further, at the level of the diaphysis, tissue area, cortical bone thickness, cortical bone area, and bone marrow area remain unaltered in *Emilin1*$^{-/-}$ femora (Figure S12E). Quantitative analysis shows lower trabecular number, increased trabecular spacing, and increased cortical bone area in juvenile and adult *Emilin1*$^{-/-}$ mice (Figures 8B and S12A). Three-point bending tests of all measured parameters show a significant increase in the

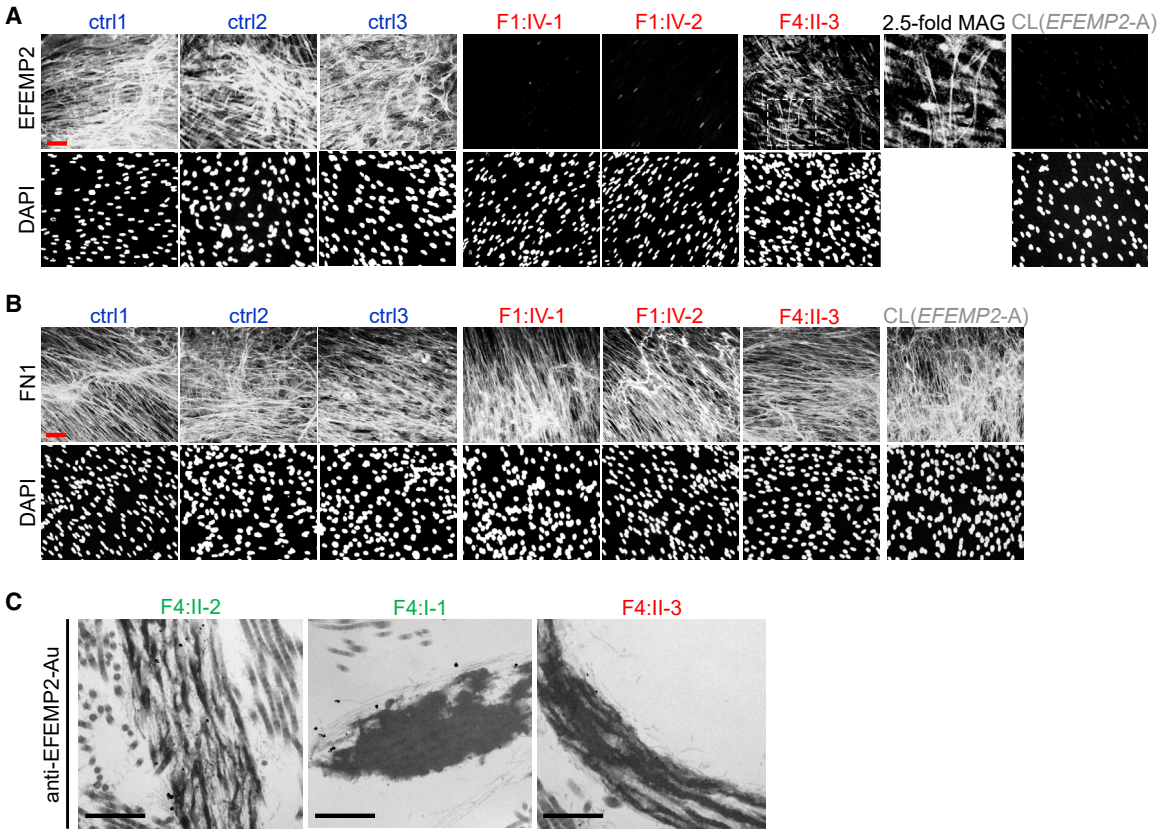

Figure 4. EMILIN1 deficiency specifically impacts EFEMP2 ECM deposition
(A and B) EFEMP2 deposition by EMILIN1-deficient fibroblast cultures is severely impaired while FN1 network assembly appears to be unperturbed. F1:IV-1 and F1:IV-2 fibroblasts show impairment of EFEMP2 deposition similar to fibroblasts from a proband with CL carrying a homozygous EFEMP2 pathogenic variant (CL(*EFEMP2*-A)). F4:II-3 cells still assemble very thin EFEMP2-positive fibers with reduced intensity (boxed area at 2.5-fold magnification). Scale bar represents 50 μm.
(C) TEM of skin biopsies subjected to immunogold labeling for EFEMP2 shows a strongly reduced presence of EFEMP2 signals within the elastic fiber/microfibril network of F4:II-3 when compared to unaffected sibling (F4:II-2) or parent (F4:I-1). Font legend: red, affected individual; green, non-affected carrier; blue, control subject.

stiffness only of the adult *Emilin1*$^{-/-}$ mouse femora (Figures 8C and S13). Interestingly, bone mineral density in perinatal (P4) *Emilin1*$^{-/-}$ femora is significantly reduced (Figure 8D), consistent with the occurrence of fractures in EMILIN1-deficient individuals within the first weeks of life (Table 1, supplemental notes, Table S1).

Discussion

Here, we report bi-allelic loss-of-function variants in *EMILIN1* as a cause for a severe vasculopathy characterized by generalized tortuosity and aneurysm formation. This recessive entity has significant overlap with ARCL1B caused by EFEMP2 deficiency and a recently described entity caused by LOX deficiency. The three conditions present with arterial tortuosity, aneurysm formation, with a propensity for arterial dissections and hypomineralization of the skeleton.[31] The skin features are pronounced in LOX deficiency due to bi-allelic *LOX* (MIM: 153455) defects and seem more variable in ARCL1B and *EMILIN1*-related disease. However, the congenital presence of pathognomonic elastic fiber defects in skin tissue due to a defect in elastogenesis, rather than secondary to elastic fiber degeneration, suggests that these entities should be classified as a form of congenital cutis laxa.[38] The clinical resemblance of these entities reflects their interconnected pathophysiology since we observed that EMILIN1 deposition is upstream of EFEMP2 in elastogenesis and, in turn, EFEMP2 is required for LOX targeting and function.[16,36] It is intriguing to speculate that LOX dysfunction is also a major player in the currently enigmatic pathophysiology of arterial tortuosity syndrome (ATS [MIM: 208050]),[39] caused by loss-of-function defects in *SLC2A10* (MIM: 606145) encoding the facilitative glucose transporter GLUT10.[40] Individuals with ATS also show generalized arterial tortuosity and aneurysm formation but an increased fracture risk has not been observed.[41] This hypothesis is further supported by a similar elastic fiber morphology in dermal biopsies of subjects with bi-allelic loss-of-function variants in *EMILIN1, EFEMP2, LOX*, and *SLC2A10*. In these biopsies, the core of the elastic fiber shows a moth-eaten appearance with elastin-depleted areas in which FMF can be observed (Figure 3C)[31,41] (unpublished data).

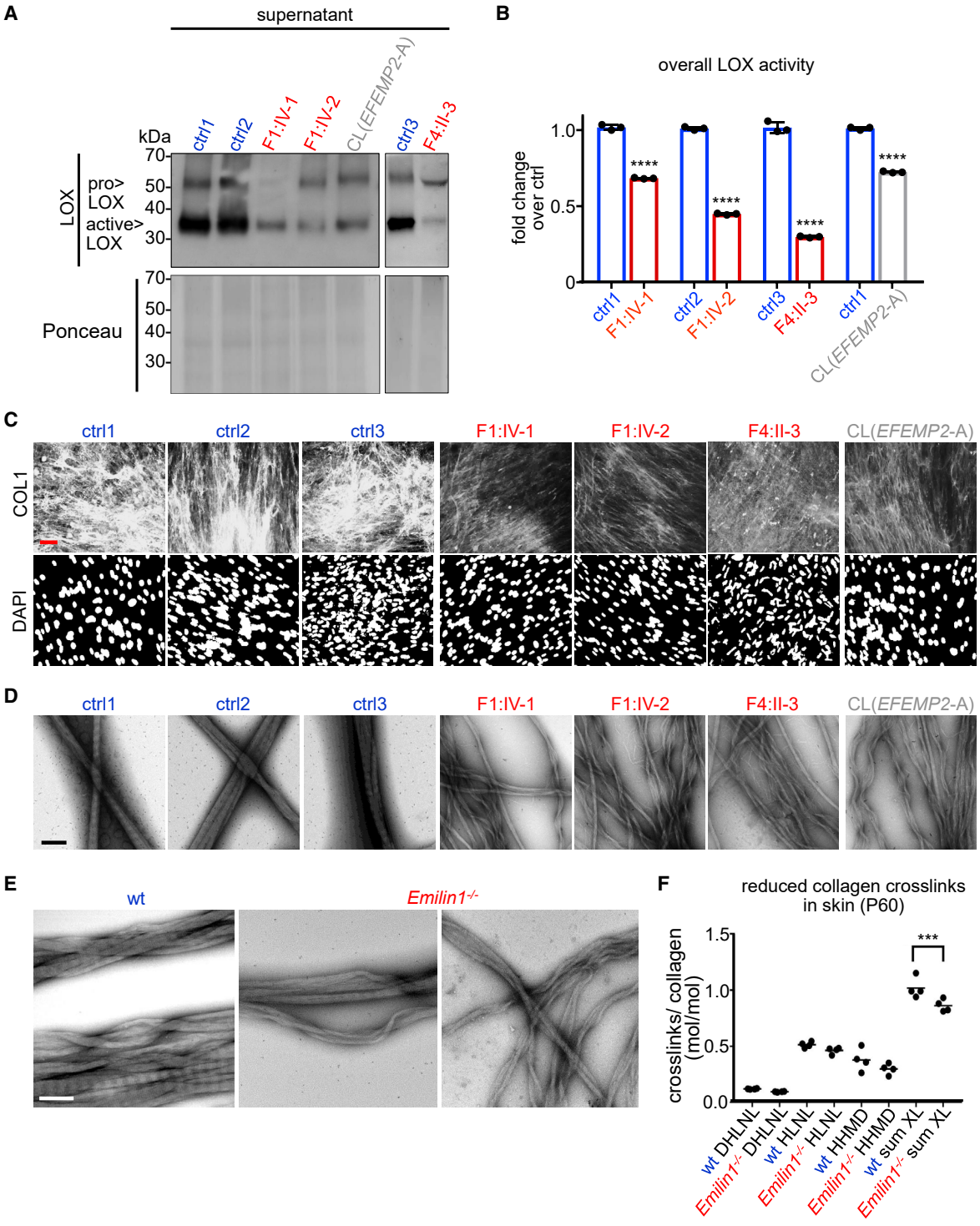

Figure 5. Loss of EMILIN1 affects LOX activity as well as collagen network assembly and crosslinking

(A) Reduced LOX levels in supernatants from F1:IV-1, F1:IV-2, F4:II-3, and EFEMP2-deficient CL(*EFEMP2*-A) fibroblast cultures shown by western blot analysis.

(B) LOX enzyme activity measurements of fibroblast cell layers from F1:IV-1, F1:IV-2, and F4:II-3 show a significant reduction of 35%–70% after 9 days of culture. LOX activity of EFEMP2-deficient CL(*EFEMP2*-A) fibroblast cultures was reduced by 30%. LOX activity analyses were performed in triplicates and data from three independent experiments are shown.

(C) Immunofluorescence analysis of collagen I networks in F1:IV-1, F1:IV-2, and F4:II-3 fibroblast cultures reveals very thin collagen I fibers at low density similar to those detected in EFEMP2-deficient cells from a CL individual (CL(*EFEMP2*-A)). Scale bar: 50 μm.

(D) Negative staining TEM of supernatants from F1:IV-1, F1:IV-2, F4:II-3, as well as EFEMP2-deficient CL(*EFEMP2*-A) fibroblasts shows a thin and curly appearance of collagen fibrils with a less distinct cross-band pattern compared to controls.

(legend continued on next page)

Our work identifies EMILIN1 as a link between elastin and collagen networks, positioning LOX function centrally in the pathogenesis of elastinopathies. This can be relevant for other monogenic disorders of the soft connective tissues, including Marfan syndrome (MIM: 154700),[42] several types of EDS,[43] congenital contractural arachnodactyly (MIM: 121050),[44] and cutis laxa[25,38] that also present with osteopenia and bone overgrowth phenotypes. Moreover, it provides an additional mechanism for variability in age-related fracture risks as reduced skin elasticity has been observed in a population with more pronounced osteopenia.[45] Indeed, EFEMP2 requires a direct interaction with EMILIN1 for assembly and deposition in the ECM of osteoblasts[5] and EMILIN1 is upregulated during postnatal cartilage maturation in murine cartilage extracts,[46,47] suggesting a role in endochondral bone growth. *Emilin1*$^{-/-}$ femora do not show any change in bone mineral density at 8 and 14 weeks of age (Figure S12C) but in the perinatal period at P4 (Figure 8D). This is consistent with observed fractures in individuals within the first period of life and appears to be a transient condition as the fracture risk seems to decrease with age in the elder individuals of family 1. Further, *Emilin1*$^{-/-}$ mice show an altered bone microarchitecture with decreased trabecular bone (Figures 8A and S12A). The trabecular bone transfers mechanical loads from the articular surface to the cortical bone and absorbs shocks.[48,49] An altered trabecular bone microarchitecture may thereby increase fracture risk in EMILIN1-deficient individuals. Indeed, fractures have not been reported in mice, which could be due to the compensatory increased cortical bone area and stiffness observed in *Emilin1*$^{-/-}$ mice femora (Figures 8B and 8C), resulting in normal bending moment values.

Mutant *EMILIN1* mRNA is predicted to undergo NMD,[50] but incomplete NMD and truncated protein production has been previously observed in fibroblasts.[40,51] EMILIN1 levels show more than 50% reduction in fibroblasts from subjects F1:IV-1 and F1:IV-2 (Figure S2A). Consequently, western blot analysis of lysates from HEK293 EBNA cells transfected with an overexpression construct carrying the identified p.Ala278Serfs*11 EMILIN1 frameshift variant confirmed reduced abundance of a truncated 25 kDa protein (Figure 2A), similarly to F1:IV-1 and F1:IV-2 cell lysates showing a minor amount of a 32 kDa protein. The truncated EMILIN1 likely undergoes intracellular breakdown since no secretion was observed in the supernatant. The 7 kDa difference between both bands of truncated EMILIN1 could relate to differences in post-translational modification such as protein glycosylation in the two employed cell culture systems.[52] Likewise, we found that the homozygous p.Gln536* variant abolishes overall EMILIN1 production in F4:II-3 skin fibroblasts, though minor protein quantities remained detectable upon immunogold EM of assembled fibers in cultures and skin biopsies (Figures S2B and 3C). This variant specific impact on remaining EMILIN1 secretion also resulted in very thin EFEMP2 fibers in F4:II-3 fibroblasts (Figure 4A) while no EFEMP2 fiber assembly was detected in F1:IV-1 and F1:IV-2 fibroblast cultures. EFEMP2 is an indispensable partner of LOX for ECM targeting and its enzymatic activity,[36] likely through interaction with the prodomain of LOX.[16] Our data clearly show that levels of active LOX were similarly significantly reduced in F1:IV-1, F1:IV-2, F4:II-3, and EFEMP2-deficient fibroblast CL(*EFEMP2*-A) cultures (Figure 5A), suggesting that EFEMP2 and EMILIN1 are both required for proper LOX function. Thereby, our data suggest that EMILIN1 affects LOX transcript levels and presence of processed LOX within the ECM (Figures S6B and S6D). The percentage of processed LOX of total LOX signals is consistently reduced in EMILIN1- and EFEMP2-deficient fibroblasts. Similarly affected LOX processing was previously reported in EFEMP2-deficient mouse skin,[53] aorta,[54] and bone.[55] Interestingly, EMILIN1-deficient human fibroblasts show a varying reduction in LOX activity (35%–70% reduction), which may be the reason for the apparent variations in elastin fiber integrity as assessed by TEM (Figure 3B). A varying severity of the moth-eaten appearance may be due to repetitive tensile forces on elastin due to the varying degree of insufficiently crosslinked elastin.

LOX modifies lysine or hydroxylysine residues in the telopeptide region of collagen molecules and promotes the formation of networks of mature collagen fibers by forming non-soluble crosslinks.[17,56] We show direct evidence of collagen defects due to defective LOX functioning in EMILIN1-deficient fibroblasts. EM analysis of EMILIN1-deficient dermal fibroblasts from affected individuals and mice reveal the presence of thin, disentwined collagen fibrils with a reduced presence of the characteristic cross-bands which was indistinguishable from fibrils produced by EFEMP2-deficient human fibroblasts (Figures 5D and 5E). This appearance is likely triggered by the acid treatment required for negative staining since less crosslinked collagen fibrils have a reduced stability at low pH.[57] Similarly, collagen fibers in *Lox*$^{-/-}$ mouse embryos are dispersed and do not form tight bundles.[58] Collagen fibril diameters in EMILIN1-deficient individuals and murine skin show an increased variability with a broader distribution shifted toward increased diameters similar to the distribution found in humans (Figure 7) and mouse models with EFEMP2

(E) Negative staining TEM of supernatants from *Emilin1*$^{-/-}$ dermal fibroblast cultures also shows a thin and curly appearance of collagen fibrils with a less distinct cross-band pattern. Scale bar in TEM micrographs: 200 nm.
(F) Crosslink analysis of *Emilin1*$^{-/-}$ mouse skin at postnatal day 60 (P60) indicates a significant reduction of the sum of identified collagen crosslinks. DHLNL, dihydroxylysinonorleucine; HLNL, hydroxylysinonorleucine; HHMD, histidinohydroxymerodesmosine. Data are expressed as mean ± SD. ***$p < 0.001$, ****$p < 0.0001$. Two-tailed unpaired t test with Welch's correction was used for statistical analysis to compare two groups.

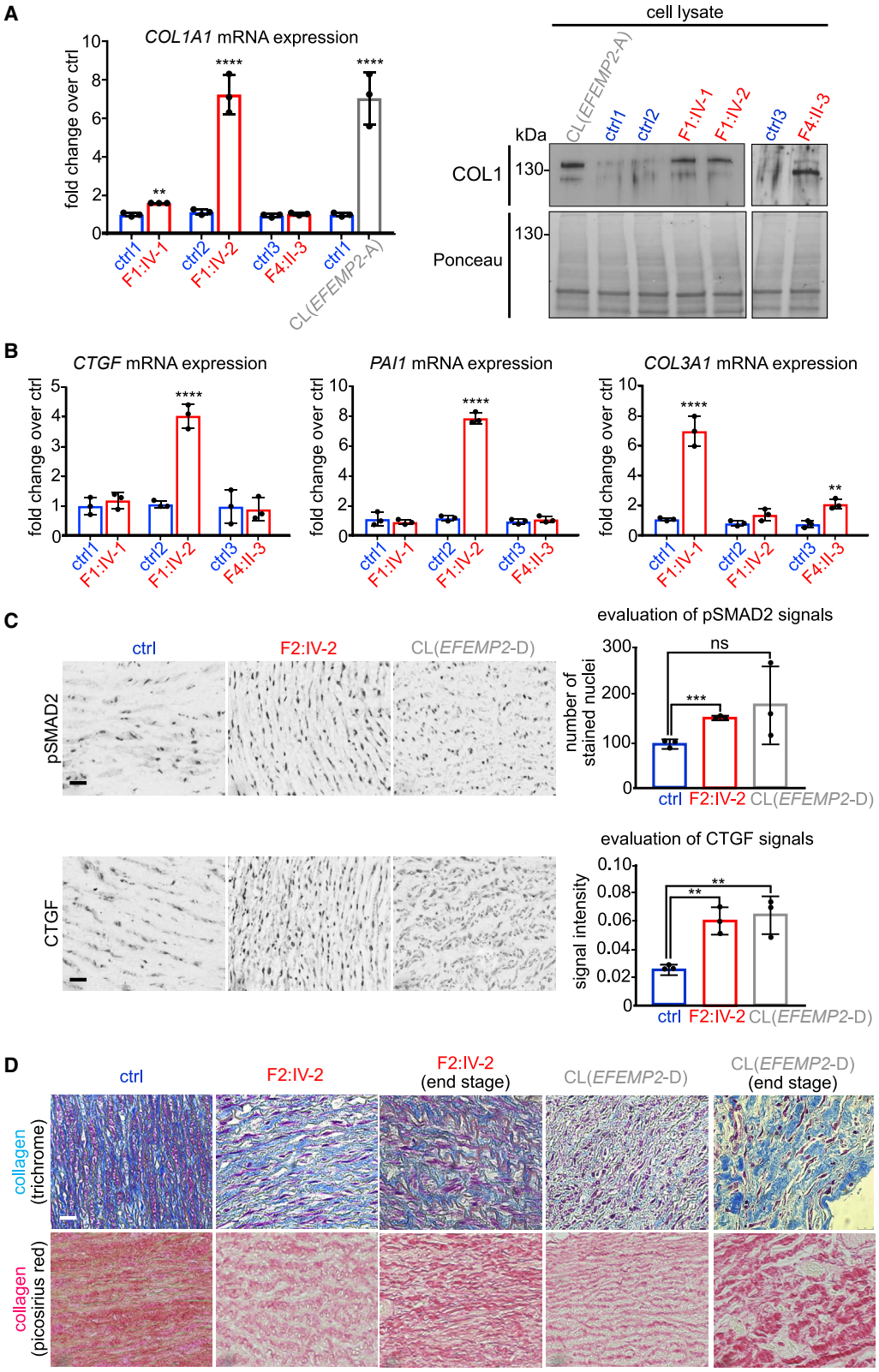

Figure 6. EMILIN1 deficiency affects collagen synthesis and TGF-β activity

(A, left) EMILIN1-deficient F1:IV-1, F1:IV-2, and EFEMP2-deficient CL(*EFEMP2*-A) fibroblasts show increased *COL1A1* transcript levels by RT-qPCR. (A, right) Increased intracellular collagen I levels in F1:IV-1, F1:IV-2, F4:II-3, and CL(*EFEMP2*-A) fibroblasts by western blot analysis.

(B) Significantly increased transcript levels of TGF-β-responsive genes *CTGF* and *PAI1* in F1:IV-2 as well as *COL3A1* in F1:IV-1 and F4:II-3 fibroblasts.

RT-qPCR analyses in (A) and (B) were performed in triplicates and data from three independent experiments are shown.

(legend continued on next page)

deficiency.[54,55] Similar to *Efemp2*$^{-/-}$ mice,[55] *Emilin1*$^{-/-}$ mouse skin also shows significant altered collagen crosslinks, and increased collagen extractability (Figures 5F and S8B). The collagen fibrils in cross-sectional view in *Emilin1*$^{-/-}$ skin merge only occasionally and thereby lose their circular shape (Figure 7C). Also, the collagen fibrils in EMILIN1-deficient human and mouse skin show less small perpendicular protrusions on transverse sections, which may reflect reduced connection to the ground substance and neighboring fibrils in the ECM. Finally, similar fibril anomalies can be generated in fibroblast cultures treated with the LOX inhibitor β-aminopropionitrile (BAPN).[59,60]

Despite defective crosslinking, collagen I production and secretion is increased in EMILIN1-deficient human dermal fibroblasts. Similar to data from siRNA-mediated EMILIN1 depletion experiments in skin fibroblasts[3] and osteoblasts,[5] fibrillin-1 and -2 as well as fibronectin fiber formation are unaltered in *EMILIN1* mutant fibroblasts (Figures 4 and S4). Moreover, ECM targeting of latent TGF-β binding proteins (LTBPs) (LTBP1 and LTBP2) is not affected in F1:IV-1, F1:IV-2, and F4:II-3 cultures (Figure S4). These findings suggest a temporal order of ECM organization by dermal fibroblasts whereby an EMILIN1 network is formed subsequent to fibronectin, fibrillin, and LTBP network formation, but prior to EFEMP2 deposition.

Increased TGF-β signaling was also reported in the context of aortic valve fibrosis in *Emilin1*$^{-/-}$ mice.[61] Furthermore, EMILIN1 was described as a negative regulator of TGF-β activity by inhibiting furin mediated cleavage of the mature TGF-β ligand from the proTGF-β precursor via direct interactions with its EMI domain.[8] Since aberrantly increased TGF-β induced abnormal collagen deposition in the aortic valve of *Emilin1*$^{-/-}$ mice,[61] it may contribute to the observed bulk of disorganized interstitial collagen in the adventitia and aortic wall of EMILIN1-deficient individuals and mice (Figures 6D and S10), similarly to the abnormal collagen deposits observed in the aortic sections of a EFEMP2-deficient CL individual (Figure 6D). Nevertheless, our findings on altered TGF-β signaling show divergent downstream alterations in different EMILIN1-deficient human fibroblast cultures (Figures 6A and 6B). Further (*in vivo*) confirmation may clarify how these mechanisms contribute to abnormal collagen distribution in EMILIN1- and EFEMP2-deficient states during initial stages of ECM deposition.

Currently, it is unclear how EMILIN1 deficiency affects *LOX* transcript levels, especially since our data show variant-specific effects of different *EMILIN1* mutations. EMILIN1 is known to bind α4 and α9β1 integrins through its gC1q domain.[62,63] Whether these interactions trigger intracellular signaling necessary for *LOX* expression, or whether intracellular EMILIN1 is required for *LOX* expression remains to be answered. Alternatively, EMILIN1 might affect *LOX* expression indirectly by altering other proteins necessary for *LOX* expression. The consistently observed higher levels of secreted cartilage oligomeric matrix protein (COMP) in EMILIN1-deficient fibroblasts may provide a possible link between reduced LOX levels and increased collagen production. COMP is an extracellular glycoprotein that belongs to the thrombospondin gene family[64] and is mainly present in cartilage, tendon, ligament, bone, and smooth muscle cells.[65,66] COMP not only orchestrates the formation of a functional collagen fibril network in the ECM, but also forms an intracellular complex with collagens that is necessary for collagen secretion.[37] Elevated COMP levels are found in pathologies associated with fibrosis.[67–69] Furthermore, COMP is upregulated in photoaged skin and correlates with increased TGF-β activity and elastic fiber damage.[70] Therefore, elastic fiber deficiency and overproduction and secretion of collagen in EMILIN1-deficient cells might also increase COMP secretion. Alternatively, members of the thrombospondin family including thrombospondin-1 (TSP-1) are involved in proLOX production and processing,[71,72] necessary for collagen crosslinking.[72] Hence, increased COMP levels could be a cause or a consequence of reduced proLOX abundance.

In contrast to human cells, murine *Emilin1*$^{-/-}$ dermal fibroblasts show strongly reduced but detectable levels of EFEMP2 that was more extractable (Figures S7A and S7B), indicating improper assembly and defective anchorage in the ECM *in vivo*. It could be hypothesized that the observed interspecies differences rely on functional redundancy of other EMILINs. Indeed, all EMILINs contain an EMI domain[4] and are present in the postnatal aorta of mice.[73] The same mechanisms may also explain why previous reports on the cardiovascular presentation in *Emilin1*$^{-/-}$ mice indicate a high systolic blood pressure,[8,74] aortic valve disease, and elastic fiber defects,[61] but no tortuosity or aneurysms. This illustrates the limitations of *Emilin1*$^{-/-}$ mice as an animal model for studying the molecular mechanisms underlying aortic disease in human *EMILIN1* deficiency. Nevertheless, the identified *in vitro* and *in vivo* alterations in EFEMP2 might explain, at least in part, the CL-like features in the identified individuals with *EMILIN1* pathogenic variants.

(C) Increased signals of phospho-SMAD2 (pSMAD2) and CTGF in the aortic walls of F2:IV-2 and CL(*EFEMP2*-D). Scale bar, 25 μm.
(D) Increased collagen deposition within the expanded intralaminar spaces of aortic wall from F2:IV-2 by trichrome and picrosirius red staining. Detected collagen shows either a diffuse, loosely packed, or bulky appearance which is similar to the collagen distribution within the aortic wall of CL(*EFEMP2*-D). Scale bar, 25 μm. Data are expressed as mean ± SD. *$p < 0.05$, **$p < 0.01$, ***$p < 0.001$, ****$p < 0.0001$.
Two-tailed unpaired t test with Welch's correction was used for statistical analysis in (A) and (B). ANOVA (analysis of variance) and subsequent Bonferroni multiple comparison post-tests were used for statistical analysis in (C).

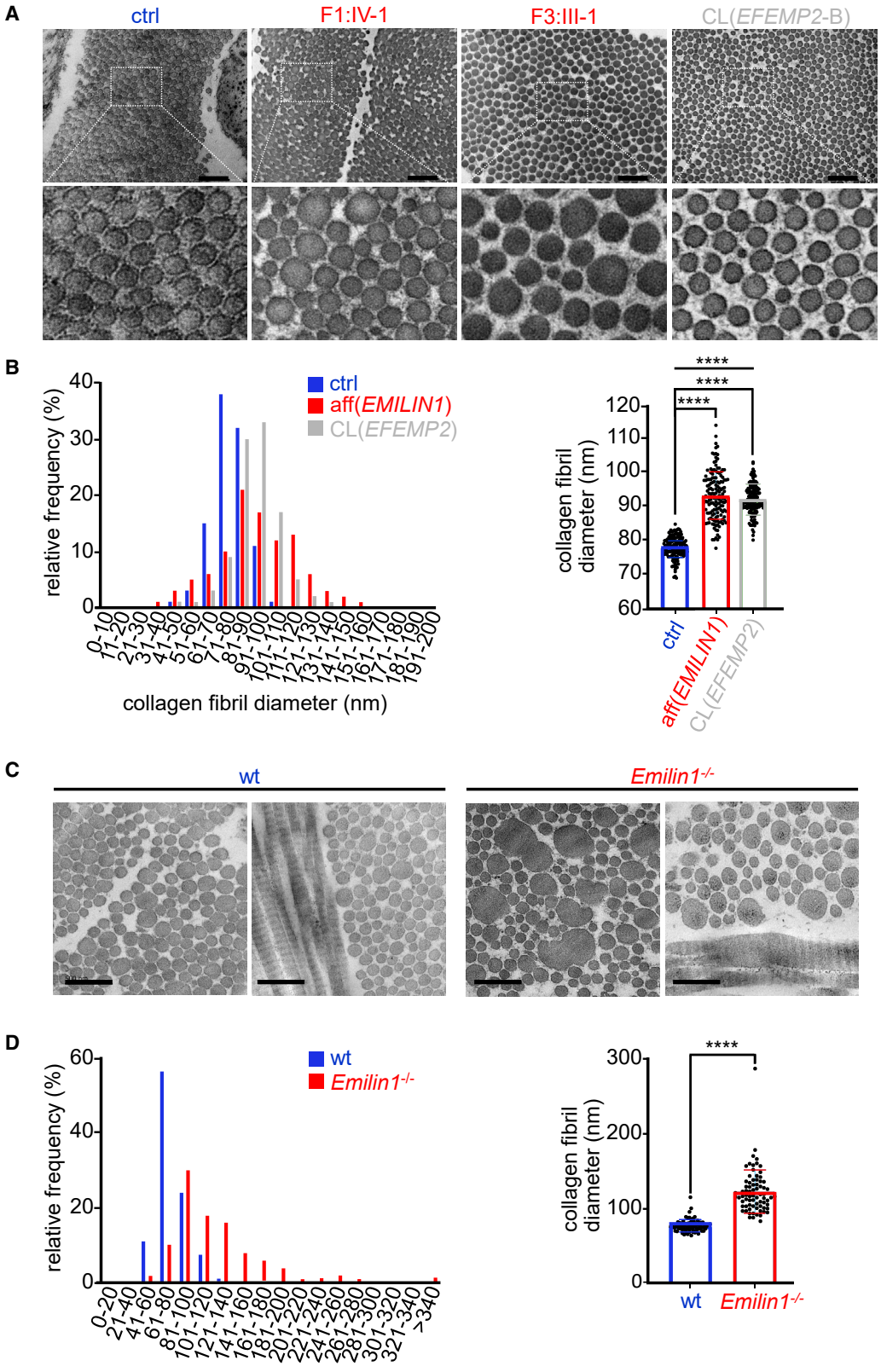

Figure 7. EMILIN1 deficiency affects collagen fibril formation

(A) TEM micrographs showing variable collagen fibril size in skin from affected individuals F1:IV-1 and F3:III-1 (aff((*EMILIN1*)), as well as from a CL proband with EFEMP2 deficiency (CL(*EFEMP2*-B)) when compared to control. Scale bars, 500 nm.

(B, left) Histograms representing collagen fibril diameter measurements. (B, right) Quantification of collagen fibril diameters in skin from F1:IV-1 and F3:III-1 as well as CL(*EFEMP2*) (CL(*EFEMP2*-B) and CL(*EFEMP2*-C) combined) indicates a wider distribution shifted toward higher abundance of collagen fibrils with larger and more variable diameter.

(legend continued on next page)

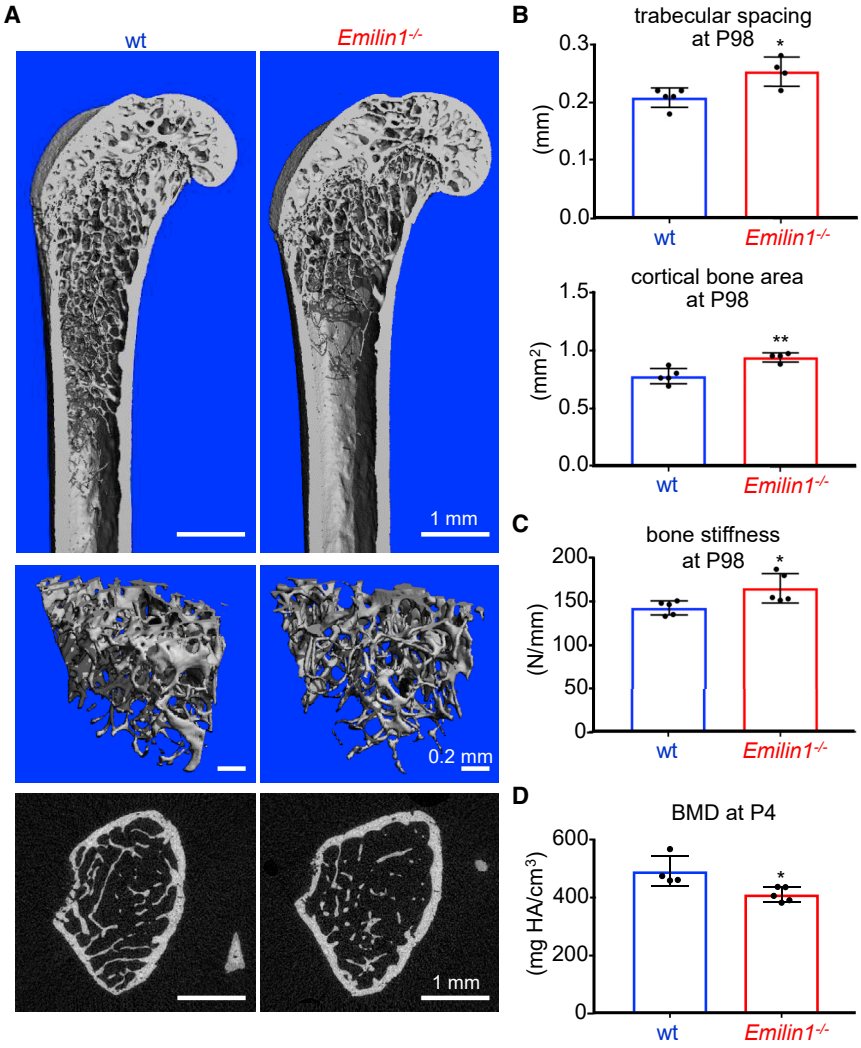

Figure 8. EMILIN1 is required for proper bone structure in mice

(A, top) Representative microCT images near the distal femoral metaphyseal region. (A, middle) magnified area and (A, bottom) corresponding cross-sectional view of adult *Emilin1*$^{-/-}$ mouse femur diaphysis at 14 weeks of age (P98) showing decreased trabecular bone.

(B) Quantitative micro-CT analysis shows increased trabecular spacing, and increased cortical bone area in *Emilin1*$^{-/-}$ mice femora at P98.

(C) Three-point-bending test shows a significant increase in stiffness of *Emilin1*$^{-/-}$ mouse femora at P98.

(D) Bone mineral density is significantly reduced in femora of *Emilin1*$^{-/-}$ mice at P4. Data are expressed as mean ± SD. *$p < 0.05$, **$p < 0.01$. Two-tailed unpaired t test with Welch's correction was used for statistical analysis.

Previously, heterozygous *EMILIN1* missense variants affecting the signal peptidase cleavage site and coiled-coil region have been identified in generalized connective tissue disease and peripheral motor neuropathy, respectively,[18,19] suggesting an autosomal-dominant transmission pattern. In contrast, our results clearly indicate a loss-of-function mechanism compatible with autosomal-recessive disease. In our study, all carriers of a heterozygous *EMILIN1* variant did not show peripheral neuropathy, and echocardiography was normal. Whether these differences are due to variant-specific consequences or whether heterozygous missense variants in EMILIN1 may result in a mild, low-penetrant phenotype remains to be established. In support of the latter, individuals with a heterozygous loss-of-function variant in *LOX* may also present with an aortic phenotype,[75] while parents of individuals with homozygous *LOX* missense variants were reportedly normal.[31]

In conclusion, we report a cutis laxa syndrome with arterial tortuosity, aneurysm formation, and osteopenia caused by bi-allelic loss-of-function variants in *EMILIN1*. We provide a model on the functional interdependence of elastic fibers and the collagen network. In this model, EMILIN1 serves a dual function in elastic fiber and collagen fiber formation. Thereby, EMILIN1 not only assists in EFEMP2 and tropoelastin deposition onto the FMF scaffold during elastogenesis, but also targets LOX via EFEMP2 to collagen fibers in order to establish critical collagen crosslinks.

Data and code availability

There are restrictions to the availability of the exome data of the analyzed individuals due to patient protection regulation by the IRB. ClinVar accession numbers of identified gene variants are: VCV001344492.26 (c.119dup), VCV001527981.1 (c.151del), VCV001527980.1 (c.831dup), VCV001343813.1 (c.1606C>T), and VCV001343812.1 (c.2457_2482dup). The published article includes all other datasets generated or analyzed during this study.

(C) TEM micrographs obtained from *Emilin1*$^{-/-}$ mouse skin at 12 weeks of age shows abnormal appearance of collagen fibrils with wider diameter. Scale bar, 500 nm.

(D) Quantification of collagen diameters in *Emilin1*$^{-/-}$ skin at 12 weeks of age indicated increased presence of collagen fibrils with larger diameter. (Left) Histogram representing collagen fibril diameter measurements on TEM micrographs from *Emilin1*$^{-/-}$ and wild-type mouse skin. (right) Quantification of measured collagen fiber diameters obtained from TEM analysis of *Emilin1*$^{-/-}$ and wild-type mouse skin. Data are expressed as mean ± SD. ****$p < 0.0001$. ANOVA and subsequent Bonferroni multiple comparison post-tests were used for statistical analysis.

Supplemental information

Supplemental information can be found online at https://doi.org/10.1016/j.ajhg.2022.10.010.

Acknowledgments

Mass spectrometric analysis and statistical evaluation was performed by Dr. Stefan Müller (CECAD Proteomics Facility). TEM-analysis of murine samples was carried out by Beatrix Martiny, C.S.A., and G.S. in the CECAD Imaging Facility. TEM-analysis of human samples was conducted by M.D.B., F.B., A.B., and R.D.R. in the VIB-Bioimaging Core. TEM analysis of fibroblast supernatants was performed by M.M. EM analyses of biopsies from family 4 were carried out by D.R.K. We are grateful to the staff in the BioEM Lab, Biozentrum, University of Basel, and the Core Facility for Integrated Microscopy (CFIM), Panum Institute, University of Copenhagen, for providing highly innovative environments for electron microscopy. We thank Carola Alampi (BioEM lab), Mohamed Chami (BioEM lab), and Klaus Qvortrup (FCIM) for practical help with electron microscopy. Funding for this study was provided by the Deutsche Forschungsgemeinschaft (DFG, German Research Foundation) project numbers 397484323 (TRR 259/B09), 73111208 (SFB 829/B12), and 384170921 (FOR2722/B1 to R.W. and M.P., FOR2722/D1 to A.N., and FOR2722/C2 to G.S.). B.C. is a senior clinical investigator of the Research Foundation Flanders. This work was supported by grants of the Special Research Fund of Ghent University (grant 01N04516C and BOF21/GOA/019 to B.C.), a research grant G035620N of the Research Foundation - Flanders (FWO) to B.C., and a research grant of European Academy of Dermatology and Venereology (PPRC-2018-50) to B.C. Ghent University Hospital is a member of the European Reference Network for Skin Disorders (ERN-Skin), intellectual disability, tele-health, autism and congenital abnormalities (ERN-ITHACA) and vascular abnormalities (VascERN).

Declaration of interests

The authors declare no competing interests.

Received: February 3, 2020
Accepted: October 20, 2022
Published: November 8, 2022

Web resources

ClinVar, https://www.ncbi.nlm.nih.gov/clinvar/
gnomAD population database, https://gnomad.broadinstitute.org/
Human Genome Variation Society guidelines, http://www.hgvs.org
MAPP, http://mendel.stanford.edu/sidowlab/downloads/MAPP/index.html
OMIM, https://omim.org/
PhD-SNP, http://snps.biofold.org/phd-snp/phd-snp.html
Polyphen-2, http://genetics.bwh.harvard.edu/pph2/
REVEL, https://sites.google.com/site/revelgenomics/
SIFT, https://sift.bii.a-star.edu.sg/
SNAP, https://www.rostlab.org/services/SNAP/

References

1. Schmelzer, C.E.H., Hedtke, T., and Heinz, A. (2020). Unique molecular networks: Formation and role of elastin cross-links. IUBMB Life *72*, 842–854.
2. Bressan, G.M., Daga-Gordini, D., Colombatti, A., Castellani, I., Marigo, V., and Volpin, D. (1993). Emilin, a component of elastic fibers preferentially located at the elastin-microfibrils interface. J. Cell Biol. *121*, 201–212.
3. Schiavinato, A., Keene, D.R., Wohl, A.P., Corallo, D., Colombatti, A., Wagener, R., Paulsson, M., Bonaldo, P., and Sengle, G. (2016). Targeting of EMILIN-1 and EMILIN-2 to Fibrillin Microfibrils Facilitates their Incorporation into the Extracellular Matrix. J. Invest. Dermatol. *136*, 1150–1160.
4. Colombatti, A., Spessotto, P., Doliana, R., Mongiat, M., Bressan, G.M., and Esposito, G. (2011). The EMILIN/Multimerin family. Front. Immunol. *2*, 93.
5. Schiavinato, A., Keene, D.R., Imhof, T., Doliana, R., Sasaki, T., and Sengle, G. (2017). Fibulin-4 deposition requires EMILIN-1 in the extracellular matrix of osteoblasts. Sci. Rep. *7*, 5526.
6. Zanetti, M., Braghetta, P., Sabatelli, P., Mura, I., Doliana, R., Colombatti, A., Volpin, D., Bonaldo, P., and Bressan, G.M. (2004). EMILIN-1 deficiency induces elastogenesis and vascular cell defects. Mol. Cell Biol. *24*, 638–650.
7. El-Hallous, E., Sasaki, T., Hubmacher, D., Getie, M., Tiedemann, K., Brinckmann, J., Bätge, B., Davis, E.C., and Reinhardt, D.P. (2007). Fibrillin-1 interactions with fibulins depend on the first hybrid domain and provide an adaptor function to tropoelastin. J. Biol. Chem. *282*, 8935–8946.
8. Zacchigna, L., Vecchione, C., Notte, A., Cordenonsi, M., Dupont, S., Maretto, S., Cifelli, G., Ferrari, A., Maffei, A., Fabbro, C., et al. (2006). Emilin1 links TGF-beta maturation to blood pressure homeostasis. Cell *124*, 929–942.
9. Callewaert, B., Renard, M., Hucthagowder, V., Albrecht, B., Hausser, I., Blair, E., Dias, C., Albino, A., Wachi, H., Sato, F., et al. (2011). New insights into the pathogenesis of autosomal-dominant cutis laxa with report of five ELN mutations. Hum. Mutat. *32*, 445–455.
10. Szabo, Z., Crepeau, M.W., Mitchell, A.L., Stephan, M.J., Puntel, R.A., Yin Loke, K., Kirk, R.C., and Urban, Z. (2006). Aortic aneurysmal disease and cutis laxa caused by defects in the elastin gene. J. Med. Genet. *43*, 255–258.
11. Tassabehji, M., Metcalfe, K., Hurst, J., Ashcroft, G.S., Kielty, C., Wilmot, C., Donnai, D., Read, A.P., and Jones, C.J. (1998). An elastin gene mutation producing abnormal tropoelastin and abnormal elastic fibres in a patient with autosomal dominant cutis laxa. Hum. Mol. Genet. *7*, 1021–1028.
12. Urban, Z., Gao, J., Pope, F.M., and Davis, E.C. (2005). Autosomal dominant cutis laxa with severe lung disease: synthesis and matrix deposition of mutant tropoelastin. J. Invest. Dermatol. *124*, 1193–1199.
13. Hucthagowder, V., Sausgruber, N., Kim, K.H., Angle, B., Marmorstein, L.Y., and Urban, Z. (2006). Fibulin-4: a novel gene for an autosomal recessive cutis laxa syndrome. Am. J. Hum. Genet. *78*, 1075–1080.
14. Renard, M., Holm, T., Veith, R., Callewaert, B.L., Adès, L.C., Baspinar, O., Pickart, A., Dasouki, M., Hoyer, J., Rauch, A., et al. (2010). Altered TGFbeta signaling and cardiovascular manifestations in patients with autosomal recessive cutis laxa type I caused by fibulin-4 deficiency. Eur. J. Hum. Genet. *18*, 895–901.
15. McLaughlin, P.J., Chen, Q., Horiguchi, M., Starcher, B.C., Stanton, J.B., Broekelmann, T.J., Marmorstein, A.D., McKay,

B., Mecham, R., Nakamura, T., and Marmorstein, L.Y. (2006). Targeted disruption of fibulin-4 abolishes elastogenesis and causes perinatal lethality in mice. Mol. Cell Biol. *26*, 1700–1709.
16. Horiguchi, M., Inoue, T., Ohbayashi, T., Hirai, M., Noda, K., Marmorstein, L.Y., Yabe, D., Takagi, K., Akama, T.O., Kita, T., et al. (2009). Fibulin-4 conducts proper elastogenesis via interaction with cross-linking enzyme lysyl oxidase. Proc. Natl. Acad. Sci. USA *106*, 19029–19034.
17. Vallet, S.D., and Ricard-Blum, S. (2019). Lysyl oxidases: from enzyme activity to extracellular matrix cross-links. Essays Biochem. *63*, 349–364.
18. Capuano, A., Bucciotti, F., Farwell, K.D., Tippin Davis, B., Mroske, C., Hulick, P.J., Weissman, S.M., Gao, Q., Spessotto, P., Colombatti, A., and Doliana, R. (2016). Diagnostic exome sequencing identifies a novel gene, EMILIN1, associated with autosomal-dominant hereditary connective tissue disease. Hum. Mutat. *37*, 84–97.
19. Iacomino, M., Doliana, R., Marchese, M., Capuano, A., Striano, P., Spessotto, P., Bosisio, G., Iodice, R., Manganelli, F., Lanteri, P., et al. (2020). Distal motor neuropathy associated with novel EMILIN1 mutation. Neurobiol. Dis. *137*, 104757.
20. Sengle, G., Charbonneau, N.L., Ono, R.N., Sasaki, T., Alvarez, J., Keene, D.R., Bächinger, H.P., and Sakai, L.Y. (2008). Targeting of bone morphogenetic protein growth factor complexes to fibrillin. J. Biol. Chem. *283*, 13874–13888.
21. Kobayashi, N., Kostka, G., Garbe, J.H.O., Keene, D.R., Bächinger, H.P., Hanisch, F.G., Markova, D., Tsuda, T., Timpl, R., Chu, M.L., and Sasaki, T. (2007). A comparative analysis of the fibulin protein family. Biochemical characterization, binding interactions, and tissue localization. J. Biol. Chem. *282*, 11805–11816.
22. Marshall, L.M., Carlson, E.J., O'Malley, J., Snyder, C.K., Charbonneau, N.L., Hayflick, S.J., Coselli, J.S., Lemaire, S.A., and Sakai, L.Y. (2013). Thoracic aortic aneurysm frequency and dissection are associated with fibrillin-1 fragment concentrations in circulation. Circ. Res. *113*, 1159–1168.
23. Isogai, Z., Ono, R.N., Ushiro, S., Keene, D.R., Chen, Y., Mazzieri, R., Charbonneau, N.L., Reinhardt, D.P., Rifkin, D.B., and Sakai, L.Y. (2003). Latent transforming growth factor beta-binding protein 1 interacts with fibrillin and is a microfibril-associated protein. J. Biol. Chem. *278*, 2750–2757.
24. Pilecki, B., Holm, A.T., Schlosser, A., Moeller, J.B., Wohl, A.P., Zuk, A.V., Heumüller, S.E., Wallis, R., Moestrup, S.K., Sengle, G., et al. (2016). Characterization of microfibrillar-associated Protein 4 (MFAP4) as a Tropoelastin- and Fibrillin-binding protein involved in elastic fiber formation. J. Biol. Chem. *291*, 1103–1114.
25. Pottie, L., Adamo, C.S., Beyens, A., Lütke, S., Tapaneeyaphan, P., De Clercq, A., Salmon, P.L., De Rycke, R., Gezdirici, A., Gulec, E.Y., et al. (2021). Bi-allelic premature truncating variants in LTBP1 cause cutis laxa syndrome. Am. J. Hum. Genet. *108*, 2386–2388.
26. Riedel, G., Rüdrich, U., Fekete-Drimusz, N., Manns, M.P., Vondran, F.W.R., and Bock, M. (2014). An extended DeltaCT-method facilitating normalisation with multiple reference genes suited for quantitative RT-PCR analyses of human hepatocyte-like cells. PLoS One *9*, e93031.
27. Sakai, L.Y., and Keene, D.R. (1994). Fibrillin: monomers and microfibrils. Methods Enzymol. *245*, 29–52.
28. Bober, M., Enochsson, C., Collin, M., and Mörgelin, M. (2010). Collagen VI is a subepithelial adhesive target for human respiratory tract pathogens. J. Innate Immun. *2*, 160–166.
29. Schindelin, J., Arganda-Carreras, I., Frise, E., Kaynig, V., Longair, M., Pietzsch, T., Preibisch, S., Rueden, C., Saalfeld, S., Schmid, B., et al. (2012). Fiji: an open-source platform for biological-image analysis. Nat. Methods *9*, 676–682.
30. Avery, N.C., Sims, T.J., and Bailey, A.J. (2009). Quantitative determination of collagen cross-links. Methods Mol. Biol. *522*, 103–121.
31. McKenzie, F., Mina, K., Callewaert, B., Beyens, A., Dickinson, J.E., Jevon, G., Papadimitriou, J., Diness, B.R., Steensberg, J.N., Ek, J., and Baynam, G. (2021). Severe congenital cutis laxa: Identification of novel homozygous LOX gene variants in two families. Clin. Genet. *100*, 168–175.
32. Bluhm, B., Ehlen, H.W.A., Holzer, T., Georgieva, V.S., Heilig, J., Pitzler, L., Etich, J., Bortecen, T., Frie, C., Probst, K., et al. (2017). miR-322 stabilizes MEK1 expression to inhibit RAF/MEK/ERK pathway activation in cartilage. Development *144*, 3562–3577.
33. Holzer, T., Probst, K., Etich, J., Auler, M., Georgieva, V.S., Bluhm, B., Frie, C., Heilig, J., Niehoff, A., Nüchel, J., et al. (2019). Respiratory chain inactivation links cartilage-mediated growth retardation to mitochondrial diseases. J. Cell Biol. *218*, 1853–1870.
34. Blumbach, K., Niehoff, A., Belgardt, B.F., Ehlen, H.W.A., Schmitz, M., Hallinger, R., Schulz, J.N., Brüning, J.C., Krieg, T., Schubert, M., et al. (2012). Dwarfism in mice lacking collagen-binding integrins alpha2beta1 and alpha11beta1 is caused by severely diminished IGF-1 levels. J. Biol. Chem. *287*, 6431–6440.
35. Hsu, M.K., Lin, H.Y., and Chen, F.C. (2017). NMD Classifier: A reliable and systematic classification tool for nonsense-mediated decay events. PLoS One *12*, e0174798.
36. Noda, K., Kitagawa, K., Miki, T., Horiguchi, M., Akama, T.O., Taniguchi, T., Taniguchi, H., Takahashi, K., Ogra, Y., Mecham, R.P., et al. (2020). A matricellular protein fibulin-4 is essential for the activation of lysyl oxidase. Sci. Adv. *6*, eabc1404.
37. Schulz, J.N., Nüchel, J., Niehoff, A., Bloch, W., Schönborn, K., Hayashi, S., Kamper, M., Brinckmann, J., Plomann, M., Paulsson, M., et al. (2016). COMP-assisted collagen secretion–a novel intracellular function required for fibrosis. J. Cell Sci. *129*, 706–716.
38. Beyens, A., Boel, A., Symoens, S., and Callewaert, B. (2021). Cutis laxa: A comprehensive overview of clinical characteristics and pathophysiology. Clin. Genet. *99*, 53–66.
39. Boel, A., Veszelyi, K., Németh, C.E., Beyens, A., Willaert, A., Coucke, P., Callewaert, B., and Margittai, É. (2021). Arterial tortuosity syndrome: an ascorbate compartmentalization disorder? Antioxidants Redox Signal. *34*, 875–889.
40. Coucke, P.J., Willaert, A., Wessels, M.W., Callewaert, B., Zoppi, N., De Backer, J., Fox, J.E., Mancini, G.M.S., Kambouris, M., Gardella, R., et al. (2006). Mutations in the facilitative glucose transporter GLUT10 alter angiogenesis and cause arterial tortuosity syndrome. Nat. Genet. *38*, 452–457.
41. Beyens, A., Albuisson, J., Boel, A., Al-Essa, M., Al-Manea, W., Bonnet, D., Bostan, O., Boute, O., Busa, T., Canham, N., et al. (2018). Arterial tortuosity syndrome: 40 new families and literature review. Genet. Med. *20*, 1236–1245.
42. Loeys, B.L., Dietz, H.C., Braverman, A.C., Callewaert, B.L., De Backer, J., Devereux, R.B., Hilhorst-Hofstee, Y., Jondeau, G., Faivre, L., Milewicz, D.M., et al. (2010). The revised Ghent

nosology for the Marfan syndrome. J. Med. Genet. *47*, 476–485.
43. Callewaert, B., Malfait, F., Loeys, B., and De Paepe, A. (2008). Ehlers-danlos syndromes and marfan syndrome. Best Pract. Res. Clin. Rheumatol. *22*, 165–189.
44. Meerschaut, I., De Coninck, S., Steyaert, W., Barnicoat, A., Bayat, A., Benedicenti, F., Berland, S., Blair, E.M., Breckpot, J., de Burca, A., et al. (2020). A clinical scoring system for congenital contractural arachnodactyly. Genet. Med. *22*, 124–131.
45. Piérard, G.E., Piérard-Franchimont, C., Vanderplaetsen, S., Franchimont, N., Gaspard, U., and Malaise, M. (2001). Relationship between bone mass density and tensile strength of the skin in women. Eur. J. Clin. Invest. *31*, 731–735.
46. Wilson, R., Diseberg, A.F., Gordon, L., Zivkovic, S., Tatarczuch, L., Mackie, E.J., Gorman, J.J., and Bateman, J.F. (2010). Comprehensive profiling of cartilage extracellular matrix formation and maturation using sequential extraction and label-free quantitative proteomics. Mol. Cell. Proteomics *9*, 1296–1313.
47. Wilson, R., Norris, E.L., Brachvogel, B., Angelucci, C., Zivkovic, S., Gordon, L., Bernardo, B.C., Stermann, J., Sekiguchi, K., Gorman, J.J., and Bateman, J.F. (2012). Changes in the chondrocyte and extracellular matrix proteome during postnatal mouse cartilage development. Mol. Cell. Proteomics *11*. M111.014159.
48. Mosekilde, L., Ebbesen, E.N., Tornvig, L., and Thomsen, J.S. (2000). Trabecular bone structure and strength - remodelling and repair. J. Musculoskelet. Neuronal Interact. *1*, 25–30.
49. Oftadeh, R., Perez-Viloria, M., Villa-Camacho, J.C., Vaziri, A., and Nazarian, A. (2015). Biomechanics and mechanobiology of trabecular bone: a review. J. Biomech. Eng. *137*.
50. Page, M.F., Carr, B., Anders, K.R., Grimson, A., and Anderson, P. (1999). SMG-2 is a phosphorylated protein required for mRNA surveillance in Caenorhabditis elegans and related to Upf1p of yeast. Mol. Cell Biol. *19*, 5943–5951.
51. Urbán, Z., Michels, V.V., Thibodeau, S.N., Davis, E.C., Bonnefont, J.P., Munnich, A., Eyskens, B., Gewillig, M., Devriendt, K., and Boyd, C.D. (2000). Isolated supravalvular aortic stenosis: functional haploinsufficiency of the elastin gene as a result of nonsense-mediated decay. Hum. Genet. *106*, 577–588.
52. Croset, A., Delafosse, L., Gaudry, J.P., Arod, C., Glez, L., Losberger, C., Begue, D., Krstanovic, A., Robert, F., Vilbois, F., et al. (2012). Differences in the glycosylation of recombinant proteins expressed in HEK and CHO cells. J. Biotechnol. *161*, 336–348.
53. Igoucheva, O., Alexeev, V., Halabi, C.M., Adams, S.M., Stoilov, I., Sasaki, T., Arita, M., Donahue, A., Mecham, R.P., Birk, D.E., and Chu, M.L. (2015). Fibulin-4 E57K knock-in mice recapitulate cutaneous, vascular and skeletal defects of recessive cutis laxa 1B with both elastic fiber and collagen fibril abnormalities. J. Biol. Chem. *290*, 21443–21459.
54. Papke, C.L., Tsunezumi, J., Ringuette, L.J., Nagaoka, H., Terajima, M., Yamashiro, Y., Urquhart, G., Yamauchi, M., Davis, E.C., and Yanagisawa, H. (2015). Loss of fibulin-4 disrupts collagen synthesis and maturation: implications for pathology resulting from EFEMP2 mutations. Hum. Mol. Genet. *24*, 5867–5879.
55. Sasaki, T., Stoop, R., Sakai, T., Hess, A., Deutzmann, R., Schlötzer-Schrehardt, U., Chu, M.L., and von der Mark, K. (2016). Loss of fibulin-4 results in abnormal collagen fibril assembly in bone, caused by impaired lysyl oxidase processing and collagen cross-linking. Matrix Biol. *50*, 53–66.
56. Trackman, P.C. (2016). Enzymatic and non-enzymatic functions of the lysyl oxidase family in bone. Matrix Biol. *52-54*, 7–18.
57. Russell, A.E. (1974). Effect of pH on thermal stability of collagen in the dispersed and aggregated states. Biochem. J. *139*, 277–280.
58. Mäki, J.M., Sormunen, R., Lippo, S., Kaarteenaho-Wiik, R., Soininen, R., and Myllyharju, J. (2005). Lysyl oxidase is essential for normal development and function of the respiratory system and for the integrity of elastic and collagen fibers in various tissues. Am. J. Pathol. *167*, 927–936.
59. Herchenhan, A., Uhlenbrock, F., Eliasson, P., Weis, M., Eyre, D., Kadler, K.E., Magnusson, S.P., and Kjaer, M. (2015). Lysyl oxidase activity is required for ordered collagen fibrillogenesis by tendon cells. J. Biol. Chem. *290*, 16440–16450.
60. Levene, C.I., and Gross, J. (1959). Alterations in state of molecular aggregation of collagen induced in chick embryos by beta-aminopropionitrile (lathyrus factor). J. Exp. Med. *110*, 771–790.
61. Munjal, C., Opoka, A.M., Osinska, H., James, J.F., Bressan, G.M., and Hinton, R.B. (2014). TGF-beta mediates early angiogenesis and latent fibrosis in an Emilin1-deficient mouse model of aortic valve disease. Dis. Model. Mech. *7*, 987–996.
62. Spessotto, P., Cervi, M., Mucignat, M.T., Mungiguerra, G., Sartoretto, I., Doliana, R., and Colombatti, A. (2003). beta 1 Integrin-dependent cell adhesion to EMILIN-1 is mediated by the gC1q domain. J. Biol. Chem. *278*, 6160–6167.
63. Danussi, C., Petrucco, A., Wassermann, B., Pivetta, E., Modica, T.M.E., Del Bel Belluz, L., Colombatti, A., and Spessotto, P. (2011). EMILIN1-alpha4/alpha9 integrin interaction inhibits dermal fibroblast and keratinocyte proliferation. J. Cell Biol. *195*, 131–145.
64. Adams, J.C., and Lawler, J. (2004). The thrombospondins. Int. J. Biochem. Cell Biol. *36*, 961–968.
65. Riessen, R., Fenchel, M., Chen, H., Axel, D.I., Karsch, K.R., and Lawler, J. (2001). Cartilage oligomeric matrix protein (thrombospondin-5) is expressed by human vascular smooth muscle cells. Arterioscler. Thromb. Vasc. Biol. *21*, 47–54.
66. Chen, F.H., Herndon, M.E., Patel, N., Hecht, J.T., Tuan, R.S., and Lawler, J. (2007). Interaction of cartilage oligomeric matrix protein/thrombospondin 5 with aggrecan. J. Biol. Chem. *282*, 24591–24598.
67. Vuga, L.J., Milosevic, J., Pandit, K., Ben-Yehudah, A., Chu, Y., Richards, T., Sciurba, J., Myerburg, M., Zhang, Y., Parwani, A.V., et al. (2013). Cartilage oligomeric matrix protein in idiopathic pulmonary fibrosis. PLoS One *8*, e83120.
68. Agarwal, P., Schulz, J.N., Blumbach, K., Andreasson, K., Heinegård, D., Paulsson, M., Mauch, C., Eming, S.A., Eckes, B., and Krieg, T. (2013). Enhanced deposition of cartilage oligomeric matrix protein is a common feature in fibrotic skin pathologies. Matrix Biol. *32*, 325–331.
69. Udomsinprasert, W., Angkathunyakul, N., Jittikoon, J., Chaikledkaew, U., Vejchapipat, P., Poovorawan, Y., and Honsawek, S. (2021). Cartilage oligomeric matrix protein as a marker of progressive liver fibrosis in biliary atresia. Sci. Rep. *11*, 16695.
70. Kobayashi, M., Kawabata, K., Kusaka-Kikushima, A., Sugiyama, Y., Mabuchi, T., Takekoshi, S., Miyasaka, M., Ozawa, A., and Sakai, S. (2016). Cartilage oligomeric matrix protein increases in photodamaged skin. J. Invest. Dermatol. *136*, 1143–1149.

71. Shearer, D., Mervis, M.O., Manley, E., Jr., Reddy, A.B., and Alford, A.I. (2019). TSP1 and TSP2 deficiencies affect LOX protein distribution in the femoral diaphysis and pro-peptide removal in marrow-derived mesenchymal stem cells in vitro. Connect. Tissue Res. *60*, 495–506.
72. Rosini, S., Pugh, N., Bonna, A.M., Hulmes, D.J.S., Farndale, R.W., and Adams, J.C. (2018). Thrombospondin-1 promotes matrix homeostasis by interacting with collagen and lysyl oxidase precursors and collagen cross-linking sites. Sci. Signal. *11*, eaar2566.
73. Braghetta, P., Ferrari, A., De Gemmis, P., Zanetti, M., Volpin, D., Bonaldo, P., and Bressan, G.M. (2004). Overlapping, complementary and site-specific expression pattern of genes of the EMILIN/Multimerin family. Matrix Biol. *22*, 549–556.
74. Litteri, G., Carnevale, D., D'Urso, A., Cifelli, G., Braghetta, P., Damato, A., Bizzotto, D., Landolfi, A., Ros, F.D., Sabatelli, P., et al. (2012). Vascular smooth muscle Emilin-1 is a regulator of arteriolar myogenic response and blood pressure. Arterioscler. Thromb. Vasc. Biol. *32*, 2178–2184.
75. Guo, D.C., Regalado, E.S., Gong, L., Duan, X., Santos-Cortez, R.L.P., Arnaud, P., Ren, Z., Cai, B., Hostetler, E.M., Moran, R., et al. (2016). LOX mutations predispose to thoracic aortic aneurysms and dissections. Circ. Res. *118*, 928–934.